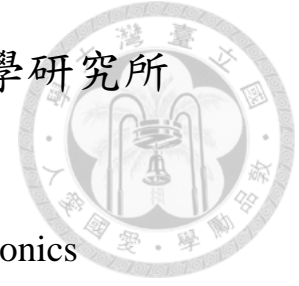


國立臺灣大學電機資訊學院光電工程學研究所

博士論文

Graduate Institute of Photonics and Optoelectronics
College of Electrical Engineering and Computer Science
National Taiwan University
Doctoral Dissertation



極紫外光數位全像顯微術

Extreme-Ultraviolet Digital Holographic Microscopy

陳秉寬

Bing Kuan Chen

指導教授：黃升龍 博士

共同指導：林俊元 博士

Advisor: Sheng-Lung Huang, Ph.D.

Co-Advisor: Jiunn-Yuan Lin, Ph.D.

中華民國 105 年 5 月

May 2016

國立臺灣大學博士學位論文

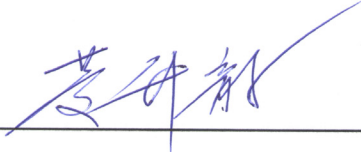
口試委員會審定書

極紫外光數位全像顯微術

Extreme-Ultraviolet Digital Holographic
Microscopy

本論文係陳秉寬君（學號 D98941016）在國立臺灣大學
光電工程學研究所完成之博士學位論文，於民國 105 年 5 月
23 日承下列考試委員審查通過及口試及格，特此證明

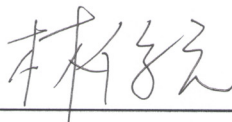
口試委員：



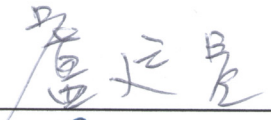
(指導教授)



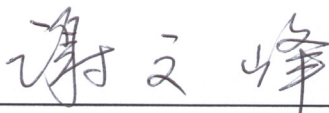
陳昭原



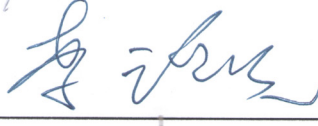
林循




詹廷恩



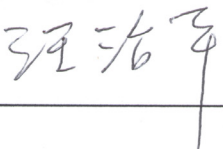
謝文峰



陳志珍



李起燿



林活華

所 長 



Acknowledgements

My sincerest gratitude goes to Professor 黃升龍 for his continuing altruistic support of my interest in high-field laser physics, and to Professor 林俊元 for introducing me into the beautiful realm of optical imaging, acquainting me with numerical skills while tackling computational simulations. I also thank Professor 陳賜原 for advising me on maintaining a 10-TW laser system, from oscillator to multi-pass amplifiers, leaving almost nothing behind. Professor 汪治平 always teaches me how to think as a scientist does, and chatting with him is full of laughter all the time. I am so lucky, having them all simultaneously as my mentors throughout my PhD studies is undoubtedly a great privilege seldom granted in other laboratories.

Every member of X-Ray Laser group, either past or current, is worthy of a Medal of Honor. We have been through a lot, like staying up till daybreak for collecting experimental data together, discussing science together, and even tasting a variety of coffee together. 余慶旻, 吳書豪, 陳泰佑 and 洪紹剛, you guys truly are warriors!

Special thanks to the dear friends we met at this lab. 周明昌 and 林秉勳 helped me get familiar with the entire x-ray laser system. 許安慶 did almost all the dirty maintenance work along with me, or even alone while I was occupied. Valuable suggestions pertaining to the maintenance of 10-TW laser system were provided by 陳彥穆 every now and then. 洪德昇 and 何彥政 assisted me in taming the unruly 100-TW laser system, and 陳惠群 covered the tedious paperwork and bureaucracy for me.

3.5-hour thesis defense is terrifyingly exhausted, being so I am grateful to each member of my thesis committee, Professor 黃升龍, Professor 林俊元, Professor 陳賜原, Professor 汪治平, Professor 李瑞光, Professor 李超煌, Professor 謝文峰 and Professor 盧廷昌, for spending their precious time participating this marathon-like small conference. They guided me to certain possible research directions with plenty of perceptive questions, and offered copious experience in academic writing.

I dedicate this thesis to my beloved family. My parents, 陳健順 and 黃量, my sister 陳育慧 and my brother 陳鈺民 are always there supporting me through thick and thin, holding us together as a solid fortress that never collapses forever and ever. In particular, I am indebted to my lovely wife 李孟芬 for taking care of everything during my long PhD journey. When I got frustrated, you and your miniaturized Lamborghini, Toyota Prius III, always took me to go for a drive with destination being often unspecified. Lastly, the one I could hardly forget to mention is you, hey, my little boy! Thank you for not kicking your mother that badly, implying not bullying me as well. You are on the right track so far, stay put for now, we'll talk later.



Extreme-Ultraviolet Digital Holographic Microscopy

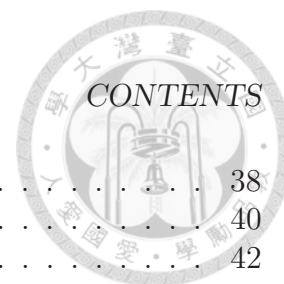
Bing Kuan Chen

May 23, 2016



Contents

Abstract	iii
List of Figures	iv
1 Coherent Amplification of Short-Wavelength Radiation	1
1.1 Challenges	1
1.2 Pumping Schemes	2
1.2.1 Optical-Field Ionization	5
1.2.2 Above-threshold-ionization heating	7
2 Extreme-Ultraviolet Laser	9
2.1 Plasma Waveguide	9
2.1.1 Guiding Condition	10
2.1.2 Axicon-Ignitor-Heater Scheme	11
2.2 High-Brightness Ni-Like Krypton Lasing at 32.8 nm	12
2.2.1 System Design and Setup	12
2.2.2 Photon Flux and Collimation	16
2.2.3 Over-Ionization	18
2.3 Summary	21
3 Holographic Processes	25
3.1 Amplitude and Phase Recording	25
3.2 Wavefront Reconstruction	26
3.3 Twin Images	28
3.4 Holographic Microscopy	28
3.4.1 Image Positions and Magnification	29
3.4.2 Equivalence of Gabor and Fourier Holography	32
4 Digital Holography	35
4.1 Discrete Fourier Transform	35
4.2 Numerical Propagation	38



4.2.1	Fresnel Transform Method	38
4.2.2	Fresnel Convolution Method	40
4.3	Recording of Digital Holograms	42
5	Twin Image Removal in Digital In-Line Holographic Microscopy	45
5.1	Overview of Twin Removal Techniques	45
5.2	Iterative Phase Retrieval	46
5.2.1	Elementary Projectors	47
5.2.2	Single-Hologram Inter-Projections Algorithm	49
5.3	Numerical Reconstructions	50
5.3.1	Proof-of-Concept Simulations	50
5.3.2	Proof-of-Concept Experiments	53
5.3.3	Extreme-Ultraviolet Digital Holographic Microscopy	55
6	Conclusion and Perspective	63
	Bibliography	65



Abstract

Bright short-wavelength coherent light sources owe their existence to the growing potential demand in both fundamental researches and industrial applications. With the advent of high-field lasers based on the chirped-pulse amplification technique, generating ultrashort coherent extreme-ultraviolet radiations with a much lower cost and even smaller size is no longer pie in the sky. In Chapter 1 and Chapter 2, we report the recent development of the extreme-ultraviolet laser at 32.8 *nm* in our laboratory. An average output of 10^{12} photons per pulse is obtained at a pump energy of less than 1 joule, reaching an unprecedentedly high energy conversion efficiency of around 10^{-5} .

Chapter 3 to Chapter 5 focus on a newly developed twin-free digital holographic microscopy using a 32.8-*nm* extreme-ultraviolet laser as the source of illumination. The computational core, single-hologram inter-projections algorithm, is numerically and experimentally proved to be capable of effectively depressing the phase ambiguity that is always encountered in the conventional reconstruction method, leading to high-fidelity object images without annoying twin disturbances. Full exemption from seeking a tight support constraint for retrieving the correct object phase also makes single-hologram inter-projections reconstruction method more fit for volumetric imaging that intrinsically requires a great amount of computational effort.

keywords: EUV laser, Optical-field ionization, Plasma waveguide, Digital holography, Twin image, Phase retrieval.



摘要

高亮度短波長同調光源因其於基礎研究與工業應用逐漸增長的需求潛力而亟待發展。隨著植基於啁頻脈衝放大技術所發展之強場雷射的誕生，以更低廉的價格與更小巧的體積產生超短同調極紫外脈衝輻射不再只是個夢想。在第一章及第二章，我們紀錄了實驗室近年在波長為 32.8 奈米極紫外光雷射的發展現況，汲發能量小於 1 焦耳的條件下每發雷射即可產生 10^{12} 顆光子，達到空前的 10^{-5} 高能量轉換效率。

第三章至第五章聚焦在以 32.8 奈米波長極紫外光雷射為照射光源的一種新發展無孿生像數位全像顯微術。其計算核心 - 「單全像互投影演算法」經數值模擬和光學實驗證明其確能有效抑制傳統全像重建術所會遭遇的相位混淆，進而回解可得無孿生像干擾的高解析物體影像。相較於傳統方法，「單全像互投影演算法」全然免除為了攫取正確物體相位所需物體輪廓的預知條件，使這新穎的演算法更加適合應用在需要大量計算量的三維體積成像。

關鍵詞: 極紫外光雷射，光場游離，電漿波導，數位全像術，孿生像，相位攫取。



List of Figures

1.1	Electromagnetic spectrum extending from VUV to soft x-ray region [1].	2
1.2	Transitions between the energy levels of (a) Ne-like and (b) Ni-like ions [2].	3
1.3	Atomic ionizations [3]. (a) Multiphoton ionization happens by the absorption of sufficient number of photons at low intensities. (b) Tunnelling ionization dominates for higher laser intensities. (c) The potential barrier is suppressed at even higher intensities, and the bound electron can escapes directly without tunneling.	6
2.1	Line focusing with an axicon [2].	11
2.2	Calculated intensity distribution of a Gaussian beam focused by an axicon [2]. (a) shows the radial intensity distribution for an incident, 55-mJ and 60-fs Gaussian beam with a 40-mm clear aperture in FWHM, while (b) shows its longitudinal counterpart.	12
2.3	Experimental layout for EUV lasing with a plasma waveguide [2]. CCD: charge-coupled device, TFP: thin-film polarizer, obj: objective, OAP: off-axis parabolic mirror, QWP: quarter-wave plate. Four diagnostic tools were adopted, which are (a) on-line imaging system, (b) relayed imaging system, (c) interferometer, (d) flat-field spectrometer and (e) far-field pattern observing system.	13



2.4	The upper half part illustrates the modified axicon-ignitor-heater pumping scheme and the relative temporal delays adopted in our experiment. Located in front of the axicon, a convex lens of 150- <i>cm</i> focal length with a hole of 2- <i>cm</i> diameter at the center is used to focus the peripheral wave fields of the waveguide-fabricating beams on the line segment matching with the slit nozzle. The tranverse distributions of electron density correspond to the temporal positions (i), (ii), (iii) and (iv) on the timeline of the upper half illustration [2].	14
2.5	Physical picture of the flat-field spectrometer. The cylindrical grating is aperiodically ruled with 1200-line/ <i>mm</i> on a concave surface [3].	15
2.6	Interferograms of the plasma taken at 10 <i>ps</i> after the pump pulse passing through the gas jet. (a) Only the pump pulse under krypton atom density $8.0 \times 10^{17} \text{cm}^{-3}$. (b) Only the pump pulse under krypton atom density $1.6 \times 10^{19} \text{cm}^{-3}$. (c) The pump pulse guided by the waveguide under krypton atom density $1.6 \times 10^{19} \text{cm}^{-3}$. The beam profiles of the pump pulse before entering and after coming out of the gas jet are shown on the two sides of each interferograms [4].	16
2.7	Number of photons for Ni-like krypton lasing at 32.8 <i>nm</i> and the corresponding beam divergence angle as a function of pump pulse energy at a krypton density of $1.6 \times 10^{19} \text{cm}^{-3}$ [5]. The temporal separation between the 47- <i>mJ</i> ignitor pulse and 208- <i>mJ</i> heater pulse was 400 <i>ps</i> . The heater-pump delay was 2.5 <i>ns</i>	17
2.8	Far-field images of the 32.8- <i>nm</i> laser beam for increasing pump pulse energies. Other parameters are the same as those in Figure 2.7. Each image adopts the same grayscale bar that scales with relative intensity.	19
2.9	(a) Spectral lines of the 32.8- <i>nm</i> laser beams for increasing pump pulse energies. (b) Angular distributions of the 32.8- <i>nm</i> laser beams for some pump energies corresponding to (a).	21
3.1	Holographic recording ¹	26
3.2	Holographic reconstruction via illumination of the original reference wave. The real image of the object is distorted by E_R^2	27

¹<http://www.flaticon.com/>



3.3	Holographic reconstruction via illumination of the conjugate reference wave. The real image of the object is undistorted while the virtual image is distorted by E_R^{*2}	28
3.4	Holographic recording and reconstruction geometries.	29
3.5	Two equivalent holographic recording schemes: (a) Fourier type with a spherical reference beam and (b) Gabor type with a planar reference wave. The black knights are the objects while the white knights stand for the corresponding twin images.	33
4.1	(a) Amplitude and (b) phase maps of the numerical diffractions with Fresnel transform method at $z = 0, 100, 200, 300 \mu\text{m}$	40
4.2	(a) Amplitude and (b) phase maps of the numerical diffractions with Fresnel convolution method at $z = 0, 100, 200, 300 \mu\text{m}$	42
4.3	Interfering geometry of two plane waves.	43
5.1	(a) Image reconstructed from a diffraction pattern with correct phases. (b) Inter-projections between two identical holograms obtained from Figure 3.5 (a) or Figure 3.5 (b).	49
5.2	Simulated hologram in (a) Fourier's; and (b) Gabor's configuration. (c) Image reconstructed by using the conventional method and (d)-(f) with SHIP method after 1, 10 and 100 iterations respectively. The white curves represent the line profiles along the white line segments.	51
5.3	(a) Simulated and (b) reconstructed phase pattern of Figure 5.2 (b); (c) The error of the reconstructed phase pattern (solid line) and the normalized intensity profile of the reference beam on the detection plane.	52
5.4	Simulated holograms under different signal-to-noise ratios (SNR) in the upper row and their corresponding reconstructions from 100 iterations of SHIP algorithm in the lower row. (a) Noise-free. (b) SNR = 40 dB. (c) SNR = 20 dB. (d) SNR = 0 dB.	53
5.5	(a) Holographic recording geometry. (b) Reconstructions of the object at different depths with the conventional method and (c) SHIP method.	54
5.6	Experimental measurements and reconstructed images with imaging magnifications of (a) $M = 5$, (b) $M = 7.5$ and (c) $M = 9.5$. From left to right : recorded holograms, reconstructions with the conventional method and reconstructions with SHIP method. The scale bars in the figures represent $50 \mu\text{m}$ in length.	55



5.7	(a) Experiment layout. CM: EUV concave mirror, FZP: Fresnel zone plate, OSA: order-sorting aperture, OBJ: object. (b) P: distance of object from the focus of the EUV laser beam, Q: distance of CCD camera from the focus of the EUV laser beam.	56
5.8	Nanostructures of the imaging Fresnel zone plate observed with a Scanning Electron Microscope under magnifications of (a) $M = 402$ and (b) $M = 1912$. (Courtesy of NanoX Lab., Academia Sinica, Taiwan)	57
5.9	(a) Digital EUV hologram of the zone plate zonal structure with a magnification of 174, and the inset is the SEM object image of the corresponding region. Patterns located by dashed ellipses are diffraction signals with weak reference illumination. (b) Reconstruction from the conventional DHM algorithm. (c) Reconstruction from the SHIP algorithm.	58
5.10	Magnification $M = 73$. Comparison of the reconstruction results from the conventional and SHIP methods. The inset at the corner of the hologram pattern is the SEM image of a carbon-foil mesh.	59
5.11	Magnification $M = 363$. Comparison of the reconstruction results from the conventional and SHIP methods. The inset at the corner of the hologram pattern is the 10/90 edge response of the SHIP intensity reconstruction.	60



Chapter 1

Coherent Amplification of Short-Wavelength Radiation

1.1 Challenges

The interesting region of the electromagnetic spectrum studied in this thesis, extreme ultraviolet (EUV), lies between the vacuum ultraviolet (VUV) and soft x-rays. As illustrated in Figure 1.1, EUV is defined here in photon energy as spanning from around 30 eV to 250 eV , with the corresponding vacuum wavelengths from around 40 nm to 5 nm [1].

EUV and soft x-ray regimes encompass an abundance of atomic resonances, making them suitable for chemical identification. Their relatively short wavelengths enable imaging applications with spatial resolutions in tens of nanometers, apparently not achievable optically. Other potential research opportunities in this spectral region can be arguably expected in the foreseeable future, and some of them are being exploited both in scientific and technological communities, for instance nanolithography in the semiconductor industry and diagnostics of high-density plasmas in the field of nuclear fusion to name a few. The demand of high-brightness coherent EUV and soft x-ray radiations fulfilling the requirements of all these modern short-wavelength applications accordingly emerges, necessitating the extension of lasing spectra from optical regime into EUV and soft x-ray range.

Pursuit of shorter-wavelength lasers has lasted till now since the first demonstration of laser came into being in 1960. The challenges facing such spectral extensions can be attributed to two facts. To begin with, inefficient cavity reflectors in EUV and soft x-ray regimes make lasing out of electromagnetic wave field oscillations inside a cavity nearly impossible [6]. Besides, upper state lifetimes of these lasing media are typically in picosec-

CHAPTER 1. COHERENT AMPLIFICATION OF SHORT-WAVELENGTH RADIATION

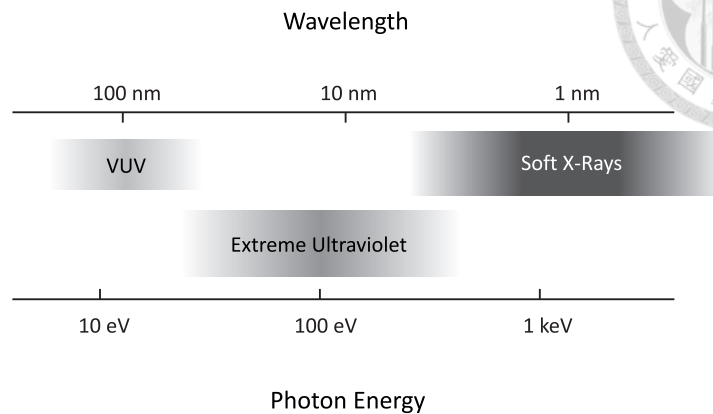


Figure 1.1: Electromagnetic spectrum extending from VUV to soft x-ray region [1].

ons or less, not able to keep up with the depopulation rates of lower states. Population inversion thus cannot sustain for many round-trip oscillations, entailing lasing operations at Amplified Spontaneous Emission (ASE) mode with a single-pass or double-pass amplification through the gain media. The other consideration is that the minimum pump power density necessary to attain a suitable gain coefficient in a naturally broadened transition scales with the lasing wavelength as λ^{-5} [7]. Pump power required for sufficiently populating ground electrons upward is drastically increasing as lasing action takes place from visible toward even shorter-wavelength regimes.

1.2 Pumping Schemes

Resonant electromagnetic radiation undergoes amplification with the passing radiation, perhaps from noisy spontaneous emission or from a seeding wave, stimulating the excited atoms within gain medium to cause transitions from their upper state to a lower state. For lasing action to occur, the upper state must be populated more than the lower state is. This population inversion contradicting the fundamental law of thermodynamics, where Boltzmann's Principle states that an upper-level population is always much smaller than a lower-level population for a collection of atoms in thermal equilibrium, should be provided from extrinsic pumping mechanism [8].

Collision excitation is the most common and easiest pumping scheme used in ion lasers at long wavelengths, whose experience was expected to pave the way for pumping short-wavelength lasers. Theoretical exploration of practicality dates back to 1970 [9, 10], while plasma with multiply charged



1.2. PUMPING SCHEMES

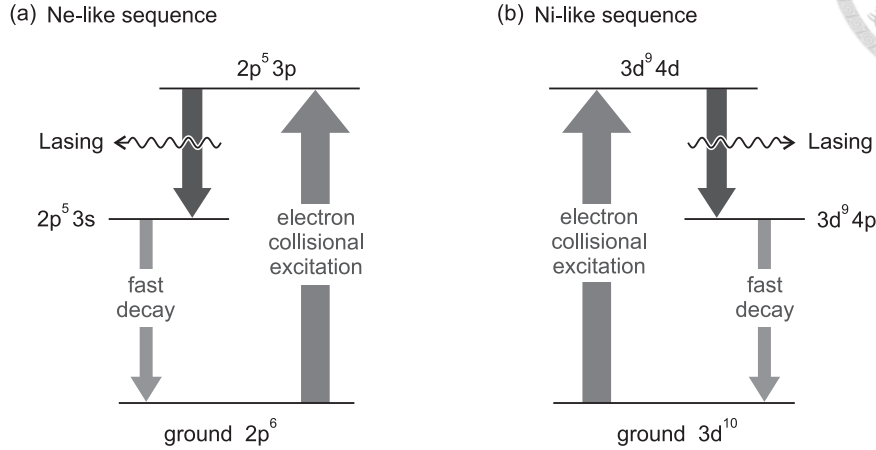


Figure 1.2: Transitions between the energy levels of (a) Ne-like and (b) Ni-like ions [2].

ions was then considered for lasers in the EUV and x-ray ranges [11]. Ions in isoelectronic sequences such as helium-like (2 bound electrons), neon-like (10 bound electrons), nickel-like (28 bound electrons) and palladium-like (46 bound electrons) all have a fully occupied outer shell, in which the symmetry of these closed shells resists to be broken and the ions with these electronic configurations are consequently hard to further ionize. This ionization bottleneck prepares copious stable ions to serve as a laser gain medium over a wide range of plasma parameters, say temperatures and densities.

EUV transition between $2p^5 3p$ and $2p^5 3s$ levels in neon-like (Ne-like) selenium and its ASE was first observed at Lawrence Livermore National Laboratory in 1984 [12]. Figure 1.2 (a) illustrates the corresponding transitions. The $n = 3$ outer levels are populated by electron collisional excitation from the ground $2p^6$ state. The population inversion then develops by the relatively rapid depopulation rate of the lower $3s$ levels through strongly dipole-allowed radiative decay to the ionic ground state.

Ne-like sequence with electron collisional pumping have been continually proved to be feasible in several EUV lasing lines [13, 14, 15, 16]. For a given lasing wavelength, however, the high degree of ionization and the consequent large pump power that is required to prepare Ne-like ions make them less attractive when compared with the ions isoelectronic with nickel (Ni-like). Depicted in Figure 1.2 (b), the $3d^9 4d$ levels are populated through direct electron collisional excitation from the ground $3d^{10}$ state of the Ni-like ions, while the lower $3d^9 4p$ level is swiftly depopulated through dipole-allowed radiative decay to $3d^{10}$.

No matter which isoelectronic sequence is considered as the gain medium

CHAPTER 1. COHERENT AMPLIFICATION OF SHORT-WAVELENGTH RADIATION

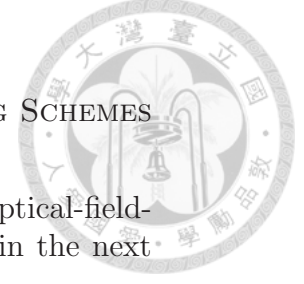


for EUV lasing, a hot dense plasma should be produced in the first place and then be followed by a process of excitation. Of the laser-induced ionization regime, three main schemes for preparing such hot dense plasmas and subsequently exciting the electrons residing in the ground-state plasmas are feasible with the help of modern laser technology, and they are briefly introduced here.

The explanation of level transitions in Ne-like and Ni-like sequences described above is nearly under steady-state condition as the pumping duration is much longer than the population inversion lifetime. In this quasi-steady-state (QSS) scheme, lasing action occurs continually as long as the plasma conditions for generating population inversion can be maintained. Nevertheless, QSS scheme usually requires large-scale pumping laser system to maintain quasi-steady state within gain medium. Typically speaking, lasers adopted for QSS scheme provide high-energy ($\approx kJ$) and relatively long ($\approx ns$) pumping pulses at a low repetition rate ($\approx \text{shot/hour}$). Such stringent performance requirements of the laser system limit the development of EUV lasers to large experimental apparatus.

Another variation named transient excitation (TE) scheme relying on the creation of a transient population inversion was proposed by Afanas'ev and Shlyaptsev in 1989 [17]. In contrast to QSS scheme that uses kilojoule laser drivers to prepare and heat the dense plasma during from several hundred picoseconds up to a few nanoseconds, TE scheme employs a nanosecond-long prepulse with an intensity of around $10^{12} W/cm^2$ to prepare a plasma with a suitable ionization state, which is followed by a heating picosecond-long pulse with an intensity of around $10^{15} W/cm^2$. The heating process of the plasma electron temperature controlled to last for shorter duration than that for the plasma to excessively ionize and further evolve utilizes the pumping energy relatively efficiently as the energy is deposited intensively within the population inversion lifetime, leading to a much larger gain coefficient than those obtained for the same transition but with QSS scheme. TE scheme owes its existence to the greatly reduced laser pump energy required for excitation. For example, the first transient collisional excitation EUV laser was demonstrated in 1997 with a few joules of pump energy deposited in a line-focused plasma, whose gain reached $19 cm^{-1}$ in the $3p - 3s$ transition of Ne-like Ti at $32.6 nm$ [18]. The same scheme has also been applied to Ni-like sequences soon after the success achieved in Ne-like sequences [19].

However promising TE scheme looks in pump energy economy, the sky is the limit for even lowering the threshold of excitation. Optical-field-ionization pumping scheme proposed by Burnett and Corkum came into being in 1989 [20]. By controlling the optical field of the interaction pulse, the atoms can be ionized to some specific ionic state, providing abundant



ground state ions for subsequently heating up. The principle of optical-field-ionization and the heating process after ionization are detailed in the next subsections.

1.2.1 Optical-Field Ionization

To ionize atoms, it seems quite natural that the photon energy $\hbar\omega$ of the interaction pulse should be higher than the electron binding potential U_i of the atoms. The photon is absorbed, leaving an ejected electron carrying the final kinetic energy E_k according to Einstein's photoelectric equation

$$E_k = \hbar\omega - U_i. \quad (1.1)$$

But this is not the real story, at least incomplete. Theoretical studies tell us that even if the ionization potential is much higher than the interaction photon energy, this weak pulse from the perspective of energy could still be intense enough to create highly stripped ions as long as the pulse duration is short enough [20]. Three regimes corresponding to different strengths of the interaction laser field are depicted in Figure 1.3. A systematic way to distinguish these regimes was given by Keldysh [21] with a parameter

$$\gamma = \sqrt{\frac{U_i}{2U_p}}. \quad (1.2)$$

U_p is the quiver energy of the electron in the laser field and defined as

$$U_p = \frac{e^2}{4m_e\omega^2} |\mathbf{E}_0|^2, \quad (1.3)$$

where e and m_e are the charge and the mass of the electron, ω is the laser frequency and \mathbf{E}_0 is its electric field. The Keldysh parameter γ essentially compares the time it would take for an atom to ionize with the oscillating period of the laser field. Multiphoton ionization dominates the whole process when ionization lasts longer as compared to the field period, this is the case $\gamma > 1$ in Figure 1.3(a). Under this condition, the atom or molecule absorbs many photons almost simultaneously right before ionization is taking place.

When the ionization potential U_i is relatively smaller as compared with the quiver energy of the electron U_p , or equivalently $\gamma < 1$, ionization is governed by electron tunneling through the skewed atomic potential. The skewness of the atomic potential comes from the field suppression of the interaction laser. Figure 1.3(b) pictures the process, which is generally referred to as optical-field ionization (OFI). It is noteworthy from Eq.(1.3) that not

CHAPTER 1. COHERENT AMPLIFICATION OF SHORT-WAVELENGTH RADIATION

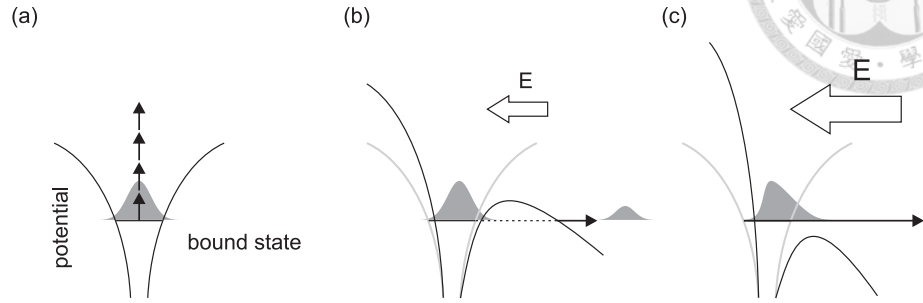


Figure 1.3: Atomic ionizations [3]. (a) Multiphoton ionization happens by the absorption of sufficient number of photons at low intensities. (b) Tunnelling ionization dominates for higher laser intensities. (c) The potential barrier is suppressed at even higher intensities, and the bound electron can escape directly without tunneling.

only is it possible to reach OFI by intense laser fields, but also by choosing low-frequency lasers for keeping γ as low as possible. To what degree can the frequency of an oscillating electric field be considered low depends on whether its period is safely longer than an orbital period of a bound electron of the atom with which it interacts [22]. An output pulse with a period $T \sim 2.6 \text{ fs}$ from a modern commercial Ti:sapphire laser oscillator can be safely classified as low-frequency field as compared to the orbital period $T \sim 150 \text{ as}$ corresponding to the Bohr radius of the hydrogen atom. Take Argon ($U_i = 15.76 \text{ eV}$) for example, an intensity of $3 \times 10^{14} \text{ W/cm}^2$ for $\gamma = 0.66$ is required for tunneling ionization [23]. In the limiting case that the laser intensity is even further increased to severely bend down the potential barrier, like that shown in Figure 1.3(c), bound electrons can directly escape from the potential trap without tunneling.

Two analytical approximations are mainly adopted to estimate the ionization rate within our interested $\gamma < 1$ regime in this thesis: Keldysh approximation [21] and Ammosov-Delone-Krainov (ADK) approximation [24]. The adiabatic assumption applying to the above two approximations limits the analyses to a premise that ionization must occur fast enough for the light field to be considered virtually static all along the process. The calculation of the ADK ionization rate takes into account certain particular atomic parameters that are neglected in the Keldysh model, achieving remarkable accuracy in comparable to some modern calculations.

From ADK theory, the instant probability of ionization for the simple



Hydrogen atom can be calculated by [25]

$$\frac{n(t)}{n_0} = 1 - \exp \left[- \int_{-\infty}^t W(t') dt' \right]. \quad (1.4)$$

W representing the ADK ionization rate takes the form of

$$W \propto U_i \exp(-4 U_i/3h\omega_t), \quad (1.5)$$

where $\omega_t = eE/(2mU_i)^{1/2}$. The whole ionization yield of an atom across the temporal profile of an incoming pulse can therefore be calculated through Eqs.(1.4) (1.5).

1.2.2 Above-threshold-ionization heating

In the long-wavelength limit, a semiclassical model, known as above-threshold-ionization (ATI), was developed to describe the interaction of a newly freed electron with the laser field [26]. At low atomic densities where other heating mechanisms are ineffective, ATI gives an efficient and controllable way of heating plasmas.

An electron gains its energy through a series of steps. To begin with, the electron is pulled out of the atomic binding potential, being free at rest. This free electron interacts with the laser field and feels an electromagnetic force exerting on it to accelerate. After the laser pulse passed by, the electron obtains some residual energy and becomes much more agitated than it initially was.

How much residual energy an electron can acquire depends on the laser field strength and phase at the time of ionization. Consider a free and rest electron just escaping from the binding potential at $t = t_0$. It looks around and immediately finds itself lying in a laser field $\mathbf{E}(t) = E_0 \cos(\omega t) \hat{x} + \alpha E_0 \sin(\omega t) \hat{y}$, where $\alpha \leq 1$ determines its polarization state. Inextricably, the electron is dragged to move along the electromagnetic field, gaining a kinetic energy averaged to be

$$K = \frac{1}{2} m_e \left\{ \langle \dot{x}^2 \rangle + \langle \dot{y}^2 \rangle \right\} \quad (1.6)$$

with the instantaneous velocities

$$\begin{aligned} \dot{x}(t) &= \frac{-eE_0}{m_e\omega} \left[\sin(\omega t) - \sin(\omega t_0) \right] \\ \dot{y}(t) &= \alpha \frac{eE_0}{m_e\omega} \left[\cos(\omega t) - \cos(\omega t_0) \right]. \end{aligned} \quad (1.7)$$

CHAPTER 1. COHERENT AMPLIFICATION OF SHORT-WAVELENGTH RADIATION



For an arbitrarily polarized laser field, Eq.(1.6) with the help of Eq.(1.7) gives the kinetic energy gained by the electron

$$\begin{aligned} K &= \frac{e^2 E_0^2}{4m_e \omega^2} \left[1 + 2 \sin^2(\omega t_0) \right] + \alpha^2 \frac{e^2 E_0^2}{4m_e \omega^2} \left[1 + 2 \cos^2(\omega t_0) \right] \\ &= \frac{e^2 E_0^2}{4m_e \omega^2} (1 + \alpha^2) + \frac{e^2 E_0^2}{2m_e \omega^2} \left[\sin^2(\omega t_0) + \alpha^2 \cos^2(\omega t_0) \right]. \end{aligned} \quad (1.8)$$

$\epsilon_q = e^2 E_0^2 (1 + \alpha^2) / 4m_e \omega^2$ is the ponderomotive energy (also known as coherent quiver energy). For interactions with ultrashort pulses, the ponderomotive energy is returned to the laser wave field as the pulse passes by and thus does not contribute to ATI at all [27]; however, the drift motion remains, in the form of the second term of Eq.(1.8). We call this residual kinetic term ATI energy

$$K_{ATI} = \frac{e^2 E_0^2}{2m_e \omega^2} \left[\sin^2(\omega t_0) + \alpha^2 \cos^2(\omega t_0) \right]. \quad (1.9)$$

It is readily seen from the above equation that a circularly polarized field is capable of producing more hot electrons than a linearly polarized field is. Calculated energy spectra of the ionized electrons for krypton by laser pulses are provided in [2], from which we observe that the energy spectrum of electrons produced from a linearly polarized field is concentrated at low energy, while the case from a circularly polarized field exhibits a broader spectrum that extends to higher electron energies.



Chapter 2

Extreme-Ultraviolet Laser

With the advent of table-top high-power laser systems and the OFI technique in the wake of it, significant progress has been made in pushing EUV lasers toward high brightness for subsequent applications and as such OFI collisional-excitation EUV lasers driven by such powerful femtosecond laser system are dramatically reduced in cost and scale.

2.1 Plasma Waveguide

Longitudinal pumping is a quite common scheme to implement traveling-wave pumping as it is able to make good use of pumping energy, but a tough conundrum emerges along the way – ionization-induced refraction largely shrinks the gain length [28]. A well-controlled waveguide can play a role in counteracting the effect of unwanted refraction by guiding the laser pulse and consequently increase the length of the gain region for lasing action. Enhancement of the OFI EUV lasing at 41.8 nm in Xe⁸⁺ in a preformed plasma waveguide driven by capillary discharge was demonstrated, which showed that the lasing signal recorded with the waveguide was approximately 4 times larger than that achieved with the gas cell [29]. After that, Mocek *et al.* utilized a 15-mm-long, multimode, gas-filled capillary tube to enhance the output of EUV lasing at 41.8 nm by an order of magnitude with respect to that from a gas cell of the same length [30, 31]. Up to 1.5×10^{11} photons per pulse was produced by using a pump energy of 1 joule.

As an alternative to capillary guiding, we have adopted optically preformed plasma waveguiding technique with a 10-terawatt (10-TW) laser system to demonstrate 400-fold enhancement of the OFI collisional-excitation EUV lasing of Ni-like krypton at 32.8 nm in a gas jet compared to that without the plasma waveguide, and the corresponding lasing photon number



reaches 8×10^{10} per pulse [4].

In the next two subsections, the basic concepts of plasma waveguide are introduced, including the working principles of pulse guiding and waveguide formation.

2.1.1 Guiding Condition

To keep a pulse in a propagating mode inside a waveguide, the on-axis delay of the phase front must be retarded more than that on the beam periphery to compensate for the divergent curvature of diffraction. With a refractive index difference $\Delta n = n(0) - n(w_0)$ between the axial (beam radius $r = 0$) and the beam periphery ($r = w_0$), a Gaussian beam traveling through a differential length δz of a graded index waveguide will simultaneously experience a focusing force due to the radial index gradient and a defocusing force due to natural diffraction. The diffractive defocusing contribution to the beam radius of curvature is $R_D = \delta z(1 + Z_R^2/\delta z^2) \approx Z_R^2/\delta z$, where Z_R is the Rayleigh range. On the other hand, the focusing part contributes to $R_F \approx w_0^2/(2\Delta n\delta z)$. The phase front can be stay flat when $R_D = R_F$, resulting in the guiding condition

$$\Delta n_g = \frac{\lambda^2}{2\pi^2 w_0^2}. \quad (2.1)$$

Any Δn smaller than Δn_g will lead to certain leaky modes of the waveguide.

The refractive index in an underdense plasma is

$$\begin{aligned} n &= \sqrt{1 - \frac{N_e}{N_{cr}}} \\ &= \sqrt{1 - \frac{4\pi e^2 N_e}{m_e \omega^2}}, \end{aligned} \quad (2.2)$$

where $N_{cr} = m_e \omega^2 / 4\pi e^2 \approx 1.74 \times 10^{21} \text{ cm}^{-3}$ for $\lambda = 810 \text{ nm}$ is the critical electron density [32]. N_e , m_e and ω are the electron density, electron mass and laser frequency, respectively. The minimum difference in electron density required to guide a beam of spot size w_0 is deduced from Eqs.(2.1) (2.2) to be

$$\Delta N_e^{min} = \frac{m_e c^2}{\pi e^2 w_0^2}. \quad (2.3)$$

For $w_0 = 10 \text{ }\mu\text{m}$, $\Delta N_e^{min} \approx 10^{18} \text{ cm}^{-3}$.

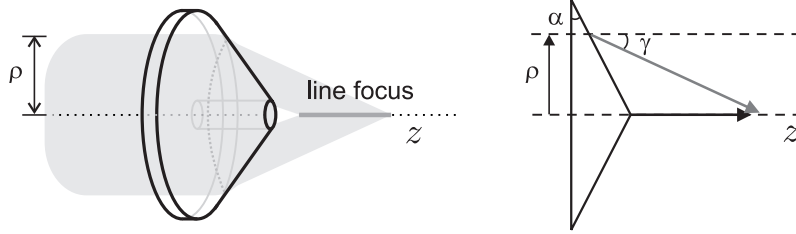


Figure 2.1: Line focusing with an axicon [2].

2.1.2 Axicon-Ignitor-Heater Scheme

A laser-ionized plasma in a gas evolves hydrodynamically into a plasma waveguide. Initially the line-focused intense pulse achieved by an axicon ionizes the neutral gas through multiphoton and OFI processes to form some seed electrons mainly on axis. Depicted in Figure 2.1, a normally incident laser beam with a radius of ρ is focused by an axicon with a base angle of α . Snell's law, $n \sin \alpha = \sin(\alpha + \gamma)$, determining the incident angle γ is then used to derive the ρ -dependent intersection distance

$$z(\rho) = \rho \left[\frac{1}{\tan \gamma} - \tan \alpha \right], \quad (2.4)$$

where n is the refractive index of the axicon and $z = 0$ is at the axicon tip. The intensity distribution of the line focus along the optical axis z is derived to be [33, 34]

$$I(z) = \frac{\pi k \sin \gamma}{2} \frac{z}{\frac{1}{\tan \gamma} - \tan \alpha} I_{\text{in}}[\rho(z)] \frac{(1 + \cos \gamma)^2}{4}. \quad (2.5)$$

A calculation example is given here to sense Eq.(2.5) a bit. Given a 55-*mJ* and 60-*fs* Gaussian beam with a 40-*mm* clear aperture to be focused by an axicon with 30° base angle and a refractive index of 1.45, a line focus of > 2 *cm* in length is brought about with an intensity distribution shown in Figure 2.2 [2].

Once the seed electrons are produced by the low-energy but high-intensity ignitor pulse, another high-energy but low-intensity pulse kicks in later to heat the preformed plasma via inverse bremsstrahlung (IB) heating, a heating process when free electrons extract energy from the laser field through electron-ion collisions [35, 36]. The heated energetic electrons collisionally ionize their adjacent ions or atoms and thus increase the electron density locally. Since the heater pulse is longer than the average electron-ion collision time (inversely proportional to the electron-ion collisional frequency), the increase in electron temperature due to IB heating leads to further ionization

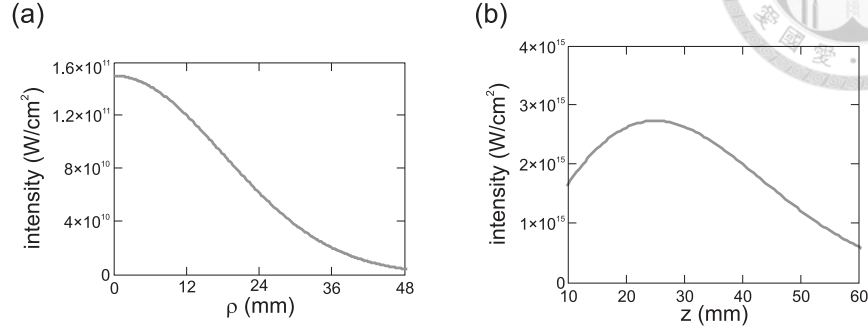


Figure 2.2: Calculated intensity distribution of a Gaussian beam focused by an axicon [2]. (a) shows the radial intensity distribution for an incident, 55- mJ and 60- fs Gaussian beam with a 40- mm clear aperture in FWHM, while (b) shows its longitudinal counterpart.

and therefore more and more electrons involve the electron-ion collisions. Such repetitive heating cycles help enhance the IB heating efficiency in a positive feedback loop, bringing about a seeded avalanche breakdown [37]. The axial hot dense lineal plasma sets to expand outward, collide with and ionize peripheral low-temperature ions and neutral atoms, which builds up an even higher-density plasma shock wave expanding at a local ion speed $v_s = \sqrt{\langle Z \rangle k_B T_e / m_i}$ as the cooler ions are pulled radially outward by the hot electrons, where $\langle Z \rangle$, k_B , T_e and m_i are the average ion charge, the Boltzmann constant, the electron temperature and the ion mass respectively. A few nanoseconds later, a cylindrically symmetric plasma column with a relatively lower on-axis electron density takes shape. If satisfying Eq.(2.3), the plasma column turns into a waveguide worthy of the name.

2.2 High-Brightness Ni-Like Krypton Lasing at 32.8 nm

2.2.1 System Design and Setup

The experiment was performed by using a Ti:sapphire laser system with 10- Hz pulse repetition rate. The laser system located in Taiwan's National Central University was based on the chirp-pulse amplification technique and consisted of three beam lines [38]. The first beam line generated laser pulses with a central wavelength of 810 nm , a minimum pulse duration of 30 fs , and a maximum peak power of 100 TW. The second beam line was of 810- nm central wavelength, 30- fs pulse duration, and 16-TW peak power. The



2.2. HIGH-BRIGHTNESS NI-LIKE KRYPTON LASING AT 32.8 NM

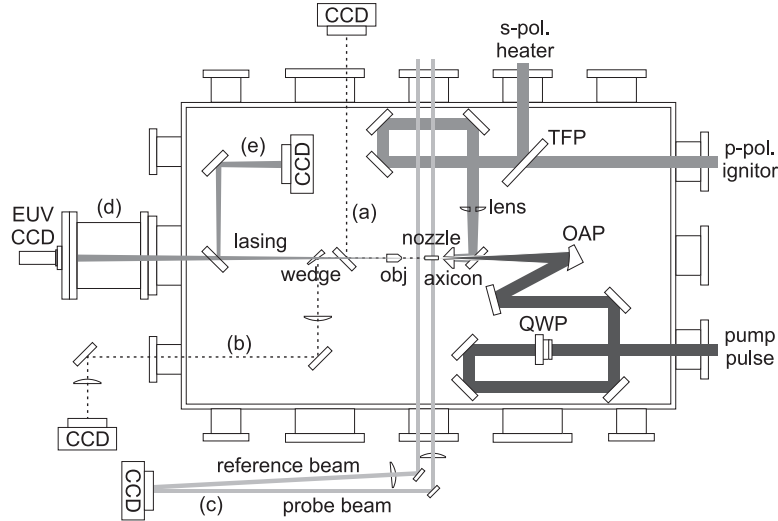


Figure 2.3: Experimental layout for EUV lasing with a plasma waveguide [2]. CCD: charge-coupled device, TFP: thin-film polarizer, obj: objective, OAP: off-axis parabolic mirror, QWP: quarter-wave plate. Four diagnostic tools were adopted, which are (a) on-line imaging system, (b) relayed imaging system, (c) interferometer, (d) flat-field spectrometer and (e) far-field pattern observing system.

third beam line was of 900- nm central wavelength, 35- fs pulse duration, and 6-TW peak power. Each laser beam can be further split into two beams with independent energy tuners, delay lines and pulse compressors. Figure 2.3 delineates the concise version of the whole experimental layout. A 30- fs , 2- J pump pulse from the 100-TW beam line was used to prepare the lasing ionization stage through optical-field ionization and heating of the plasma electrons. It was focused with an off-axis parabolic mirror of 30- cm focal length onto a krypton gas jet. The focal spot size of the pump pulse was 10- μm diameter in full width at half maximum (FWHM) with 71% energy enclosed in a Gaussian-fit profile, corresponding to a vacuum peak intensity of $4 \times 10^{19} \text{ W/cm}^2$. A motorized quarter-wave plate in the pump beam path was used to vary the pump polarization. Two laser pulses from the 16-TW beam line, referred to as the ignitor and the heater pulses, were used to fabricate the plasma waveguide. The leading 35- fs , p -polarized ignitor pulse was 47 mJ in energy and was followed after 400- ps delay by the 210- ps s -polarized heater pulse with 208- mJ energy. After combined by a thin-film polarizer, the two pulses propagated collinearly and were then focused by an axicon of 30° base angle to a line focus of $> 2\text{-}cm$ length in FWHM. The line focus overlapped with the propagation path of the pump pulse in the gas

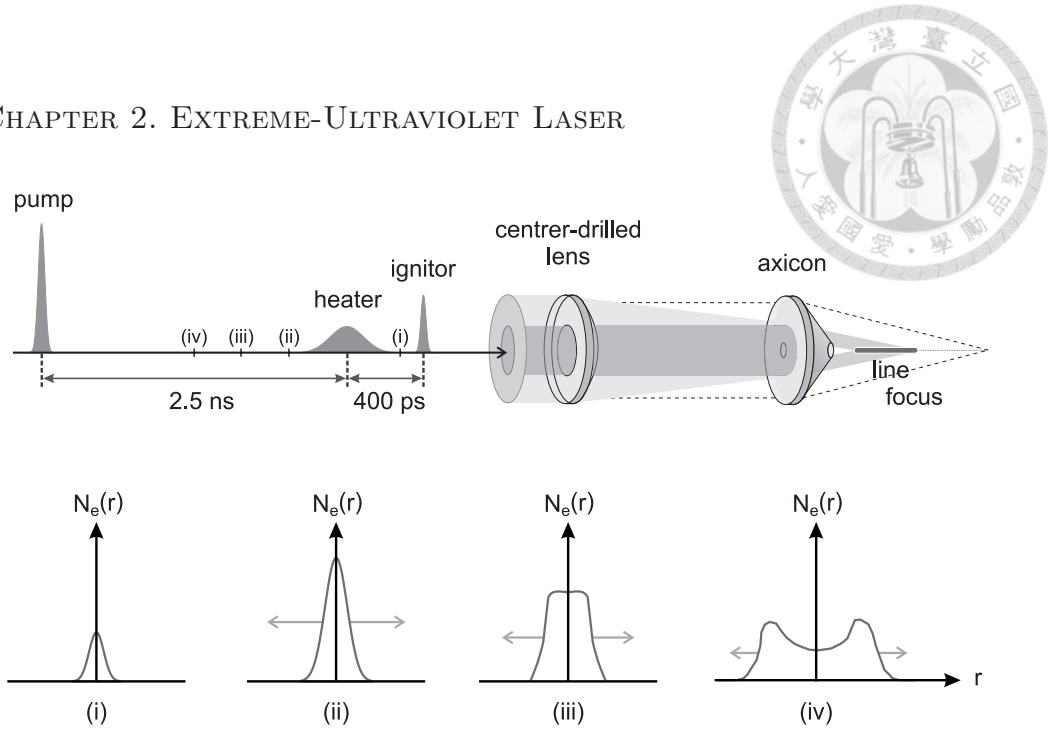


Figure 2.4: The upper half part illustrates the modified axicon-ignitor-heater pumping scheme and the relative temporal delays adopted in our experiment. Located in front of the axicon, a convex lens of 150-cm focal length with a hole of 2-cm diameter at the center is used to focus the peripheral wave fields of the waveguide-fabricating beams on the line segment matching with the slit nozzle. The transverse distributions of electron density correspond to the temporal positions (i), (ii), (iii) and (iv) on the timeline of the upper half illustration [2].

jet. A hole of 5-mm diameter at the center of the axicon allows passage of the pump pulse. To increase the efficiency of plasma waveguide fabrication, a convex lens of 150-cm focal length with a hole of 2-cm diameter at the center was installed in front of the axicon to concentrate the laser energy in a length of approximately 1 cm, matching with that of the gas jet, and to optimize the uniformity of the longitudinal intensity distribution. The modified axicon-ignitor-heater pumping scheme and the relative temporal delays of the waveguide fabricating pulses and the pump pulse are shown in Figure 2.4. Also in the figure, the chronological evolution of the radial electron density from (i) to (iv) illustrates the forming process of the plasma waveguide.

We use five optical diagnostic systems to check on every crucial step mainly during the waveguide fabrication and after EUV lasing, and they are deployed as shown in Figure 2.3. On-line imaging system uses a 20 X microscope objective to perform spatial overlaps between the waveguide-forming pulses and the pump pulse in the atmospheric environment and in the vac-

2.2. HIGH-BRIGHTNESS NI-LIKE KRYPTON LASING AT 32.8 NM

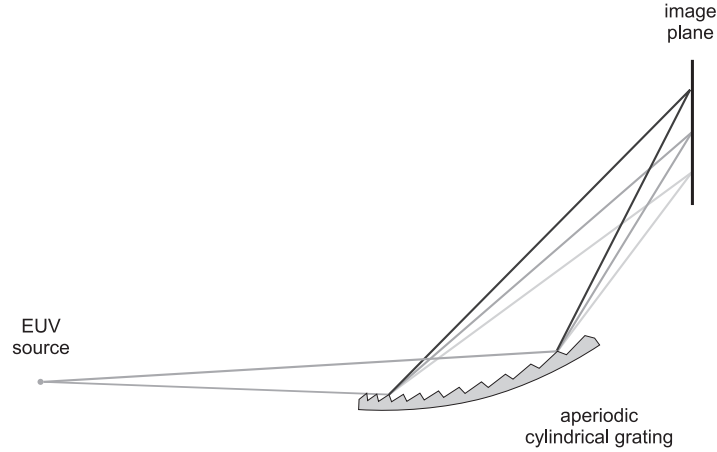


Figure 2.5: Physical picture of the flat-field spectrometer. The cylindrical grating is aperiodically ruled with 1200-line/ mm on a concave surface [3].

uum. The three-beam overlapping is imaged onto a 16-bit charge-coupled device (CCD) camera along the 1- cm -long waveguide-to-be lineal segment. A relayed imaging system consisting of a retractable wedge, a pair of lenses, an objective lens, a 40- nm bandpass filter centered at 810 nm and another 16-bit CCD camera is used to measure the spatial profile of the pump pulse at the exit of the gas jet with an imaging resolution of 5.8 μm . Mach-Zehnder interferometry measures the density distribution of electrons with two compressed pulses consisting of a reference beam and a probe beam. The probe pulse of 15- mm diameter obtained from leakage of the pump pulse at a dielectric mirror passes transversely through the cluster jet to interfere with the unperturbed reference pulse on the other 16-bit CCD camera, providing decipherable interference fringes that relates to the local electron density. The primary spectral diagnostics for EUV radiation is a flat-field grazing-incidence x-ray spectrometer that is composed of an aperiodically ruled cylindrical grating with 1200 line/ mm (001-0437, Hitachi) and a back-illuminated 16-bit x-ray CCD camera (DX420-BN, Andor Technology). The spectrometer is used to measure the spectrum and beam divergence of the EUV emission in the direction of laser propagation. As shown in Figure 2.5, such flat-field spectrometer (FFS) employs a concave grating with varied groove spacing to produce a flat image plane [39], which is exclusively useful for image acquisition of an x-ray CCD with a plane image sensor. Finally, an observing system for studying the far-field pattern of the lasing signal is introduced to evaluate the dependence of the guiding efficiency on the pump energy.

Two 0.25- μm -thick aluminum filters are used to block the transmitted

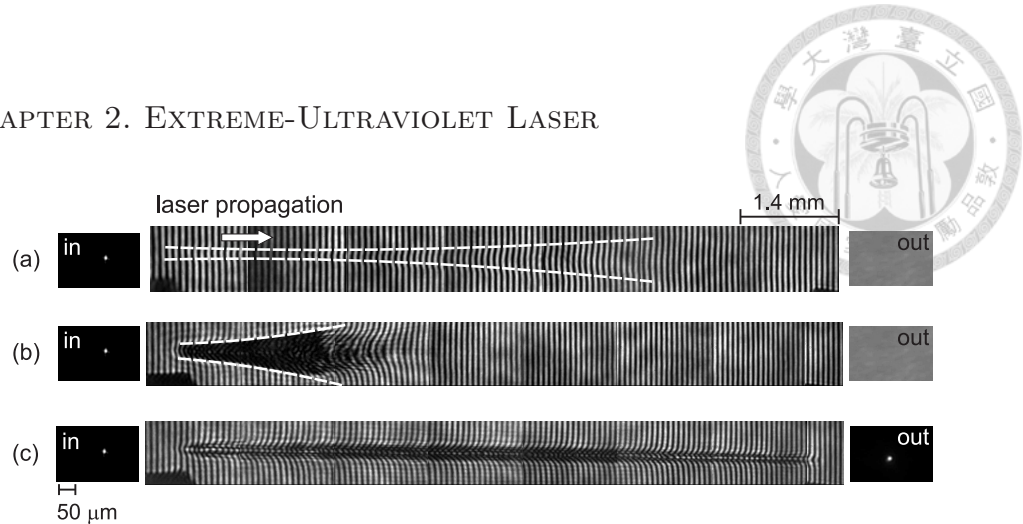


Figure 2.6: Interferograms of the plasma taken at 10 ps after the pump pulse passing through the gas jet. (a) Only the pump pulse under krypton atom density $8.0 \times 10^{17}\text{ cm}^{-3}$. (b) Only the pump pulse under krypton atom density $1.6 \times 10^{19}\text{ cm}^{-3}$. (c) The pump pulse guided by the waveguide under krypton atom density $1.6 \times 10^{19}\text{ cm}^{-3}$. The beam profiles of the pump pulse before entering and after coming out of the gas jet are shown on the two sides of each interferograms [4].

pump laser pulse and attenuate EUV emission to avoid saturating the CCD camera. A dipole magnet with a magnetic field of 0.18 T is deployed in front of the FFS to deflect the electrons emitted from the interaction region to prevent false signals in the x-ray CCD camera. From the calibrated filter transmittance, the reflectivity of the concave grating and the CCD response with respect to the target wavelength, the approximate photon number of the EUV lasing is determined.

2.2.2 Photon Flux and Collimation

Waveguiding through an optically preformed plasma channel has been shown to be promising in increasing the photon flux and improving the directionality of the EUV lasing. An instructive comparison between the results with and without the plasma waveguide is made here [4]. Without the plasma waveguide, the output EUV lasing of Ni-like krypton at 32.8 nm reached its maximum at an atom density of $8.0 \times 10^{17}\text{ cm}^{-3}$ and a pump focal position of 2.75 mm behind the entrance of the gas jet, whose pump pulse is 235 mJ in energy, 45 fs in duration and circularly polarized. The interferogram taken at 10 ps after the pump pulse passing through the gas jet is shown in Figure 2.6(a). The photon number per pulse at the 32.8-nm lasing line is 2×10^8 and the beam divergence is 15 mrad in FWHM. The interferogram in (b) was taken at the same condition as that in (a) except that the krypton



2.2. HIGH-BRIGHTNESS NI-LIKE KRYPTON LASING AT 32.8 NM

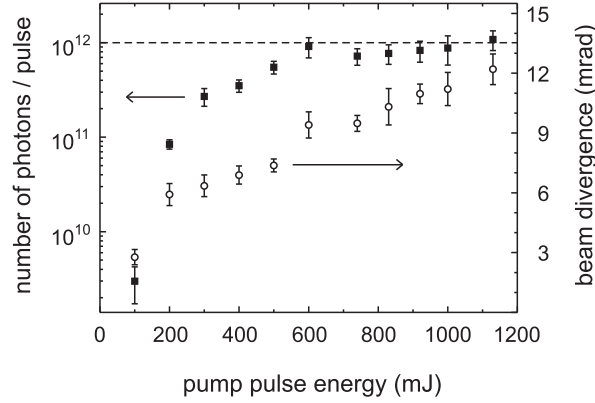
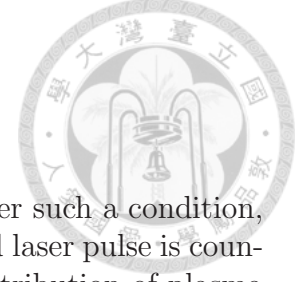


Figure 2.7: Number of photons for Ni-like krypton lasing at 32.8 nm and the corresponding beam divergence angle as a function of pump pulse energy at a krypton density of $1.6 \times 10^{19} \text{cm}^{-3}$ [5]. The temporal separation between the 47-mJ ignitor pulse and 208-mJ heater pulse was 400 ps. The heater-pump delay was 2.5 ns.

atom density was raised to $1.6 \times 10^{19} \text{cm}^{-3}$ and the pump focal position was moved to 500 μm behind the entrance of the gas jet. Increase in ion density is supposed to result in a larger lasing gain, even so the severe ionization-induced refraction drastically reduces the gain length and thus no EUV lasing was observed. The situation had been greatly changed after the introduction of a uniform plasma waveguide of 40- μm diameter and 9-mm length. It is clear from Figure 2.6(c) that the pump pulse was well guided in the plasma waveguide, with a guided beam size of smaller than 15 μm in FWHM. The output reaches 8×10^{10} photon/pulse with 10% fluctuation and the beam divergence is decreased to 5.6 mrad in FWHM with 20% fluctuation.

To exploit the potential of guiding an even intenser pump pulse, various pump energy up to 1 J per pulse were tested [5]. Still, the krypton gas jet used for this test was produced from a supersonic slit nozzle and a pulsed valve. The nozzle had a slit outlet of 10 mm in length and produced a gas jet with 9-mm flat-top region and a sharp boundary of 300 μm at both edges along the slit direction. A plasma waveguide based on the axicon-ignitor-heater scheme introduced in 2.1.2 was used to extend the gain length [40]. Laser pulses coupled into the plasma waveguide were found to be guided to



maintain a small beam size over the entire channel. Under such a condition, diffraction and ionization-induced refraction of the guided laser pulse is counteracted by the focusing effect arising from parabolic distribution of plasma electron density in the plasma waveguide. Figure 2.7 shows the number of photons for 32.8-*nm* Kr⁸⁺ lasing line with a pure-krypton plasma waveguide and the corresponding beam divergence angle as a function of pump pulse energy at a krypton density of $1.6 \times 10^{19} \text{cm}^{-3}$. All of the data points in the figure represent the average of four laser shots with error bars representing the rms error. The uniform pure krypton plasma waveguide was produced by using a 47-*mJ* ignitor pulse followed by a 208-*mJ* heater pulse with a 400-*ps* temporal separation. The delay between the heater pulse and the circularly-polarized pump pulse was 2.5 *ns*. To achieve the optimal guiding (or coupling) condition of the pump pulse, the focal position of the pump pulse was set at 500 μm behind the entrance of the gas jet. The beam profile of the pump pulse at the exit of the plasma waveguide was measured by the relayed imaging system. The data indicate that the pump pulse was well guided over the entire length of the plasma waveguide with a guided beam size of $\sim 15 \mu\text{m}$ in FWHM at various pump energy.

2.2.3 Over-Ionization

Based on the relayed imaging measurements, the efficiency of the krypton waveguide (beam energy at the exit of the waveguide divided by beam energy at the entrance of the waveguide) was estimated to be $\sim 20\%$ for pump energy $< 300 \text{ mJ}$. When pump energy is higher than 300 *mJ*, the estimation of the waveguide efficiency becomes unreliable and underestimated because strong ionization blue shift [41] reduces the portion of the broadened spectrum received by the relayed imaging system which consists of an $810 \pm 20 \text{ nm}$ bandpass filter. The strong dependence of the 32.8-*nm* laser on pump pulse energy for energies smaller than 300 *mJ* is expected due to the higher Kr⁸⁺ ion fraction, wider lasing region and longer gain length for higher pump intensity in the plasma waveguide. The declined rate of increase of lasing output at pump energies between 300 *mJ* and 600 *mJ* may be attributed to the saturated ion fraction (to unity), gain length (to the length of the plasma waveguide) and over-ionization at the center of lasing gain column. For pump energies larger than 600 *mJ*, the axial peak intensity in the waveguide channel is much higher than the ionization intensity threshold for producing Kr⁸⁺ ions ($\sim 2 \times 10^{16} \text{ W/cm}^2$), resulting in significant over-ionization along the optical axis. The maximum lasing output of $\sim 10^{12}$ photons/pulse resulting from the balance between the axial gain depletion and the increasing periph-

2.2. HIGH-BRIGHTNESS NI-LIKE KRYPTON LASING AT 32.8 NM

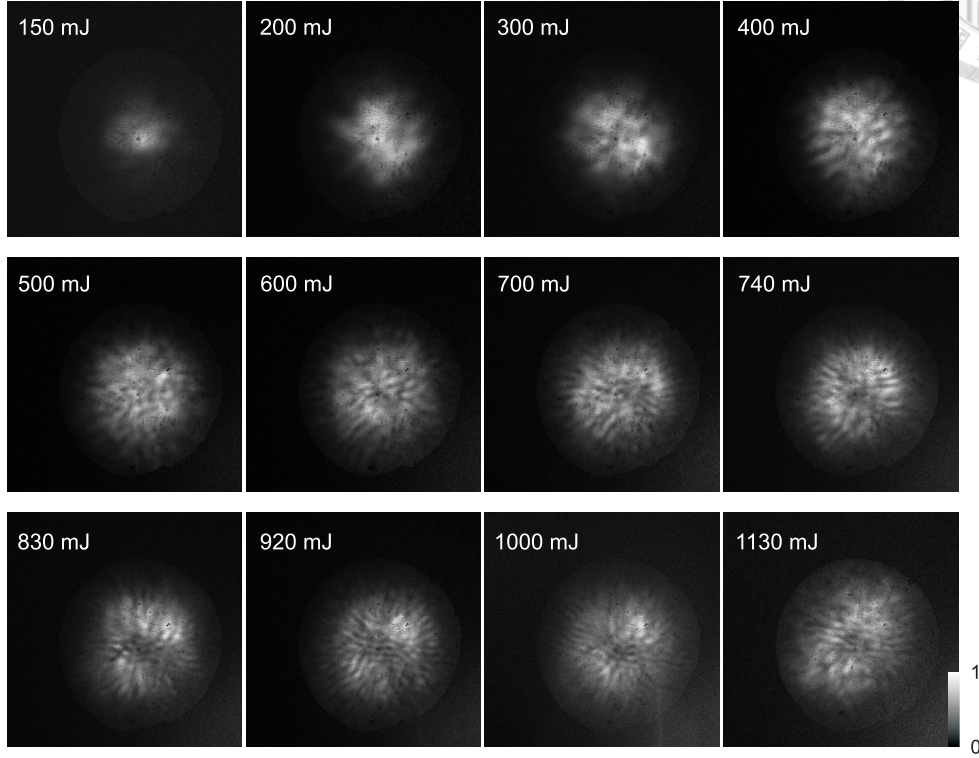
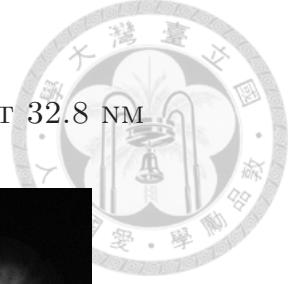


Figure 2.8: Far-field images of the 32.8-*nm* laser beam for increasing pump pulse energies. Other parameters are the same as those in Figure 2.7. Each image adopts the same grayscale bar that scales with relative intensity.

eral gain volume is reached at an energy conversion efficiency of $\sim 1 \times 10^{-5}$, and the divergence angle of which subtends about 9.4 mrad. The increasing transverse dimension of the gain volume at higher pump energy is supported by the larger lasing source sizes derived from the far-field patterns of Kr lasers described in the following context. Figure 2.7 also shows the increase of beam divergence with increasing pump pulse energies, from approximately 3 mrad for pump energy at 100 *mJ* to around 12 mrad for pump energy at 1130 *mJ*. It is noted that the beam divergence increases dramatically at pump energy larger than 600 *mJ* due to transformations of the beam profile from a single dominant peak to an annular structure.

The spatial profile of the EUV laser was characterized by a far-field imaging system consisting of two 45°, Mo/B₄C/Si EUV multilayer mirrors, two 0.25- μm -thick Al filters and an x-ray CCD with a 1024 \times 1024 array of 13- μm pixels at a distance of 65 *cm* downstream from the exit of the plasma waveguide. The EUV multilayer mirrors, served as spectral filters with relatively high reflectivities at 32.8 *nm* to prevent reflected light other than



the 32.8 *nm* from being detected, were used to redirect the EUV beam to the x-ray CCD camera as shown in Figure 2.3(e). In this study, the far-field patterns were recorded by accumulating 10 laser shots to obtain more uniform images with higher signal-to-noise ratios. Far-field images of the Kr laser at 32.8 *nm* for increasing pump energies are shown in Figure 2.8. All experimental parameters were the same as those described in 2.2.1. At pump pulse energies lower than 300 *mJ*, the far-field intensity distribution of EUV laser beam shows a narrow circular peak. As the pump pulse energy increases, the beam size defined in FWHM becomes increasingly larger and so does the corresponding beam divergence angle. Meanwhile, the far-field beam profile gradually evolves from a single dominant peak into an annular pattern starting from the vicinity of the central axis. The ring structure in the annular beam gradually moves outward to form a wider and deeper intensity valley. Figure 2.9(a) shows the spectra of the EUV laser recorded by the FFS at various pump energies, in which the direction along the abscissa represents the intensity distribution at some specific spectral line, 32.8 *nm* in this case. To quantitatively estimate the angular divergences of the EUV lasing signals corresponding to different pump energies, the divergent angles are deduced from the information provided by Figure 2.9(a) and the propagation distance to appear in Figure 2.9(b). The output photon number and beam divergence measured by both the FFS and the far-field imaging system are found to be in good agreement. It is interesting to note that the size of speckles observed in the far-field pattern decreased when the pump energy was gradually increased. This implies that Kr EUV lasers had a larger source size under higher energy pumping. The mean small speckle sizes of Kr lasers at various pump energy were measured to be 1.06 *mm* at 200 *mJ*, 0.59 *mm* at 300 *mJ*, 0.52 *mm* at 700 *mJ* and 0.38 *mm* at 1130 *mJ*, which correspond to source sizes of 20 μm , 36 μm , 41 μm and 56 μm respectively. The retrieved source sizes are well comparable with the guided beam size and the transverse dimension of the plasma waveguide. The increasing source size at higher pump energy also agrees with the wider gain regions suggested in the above discussion.

The formation of the annular EUV laser beam previously observed in capillary discharge plasma channels was due to relatively strong refraction caused by radial electron density gradients inside the plasma column [42]. In our experiment, pump pulse intensity $> 2 \times 10^{17} \text{ W/cm}^2$ (\sim the ionization threshold of Kr^{9+}) was observed at the exit of the plasma waveguide for pump pulse energy higher than 300 *mJ*. Under such experimental condition, the intensity in the pump pulse wings which is originally lower than the ionization threshold for Kr^{8+} begins to exceed the threshold and thus results in a wider gain region when the pump energy is gradually increased. However,

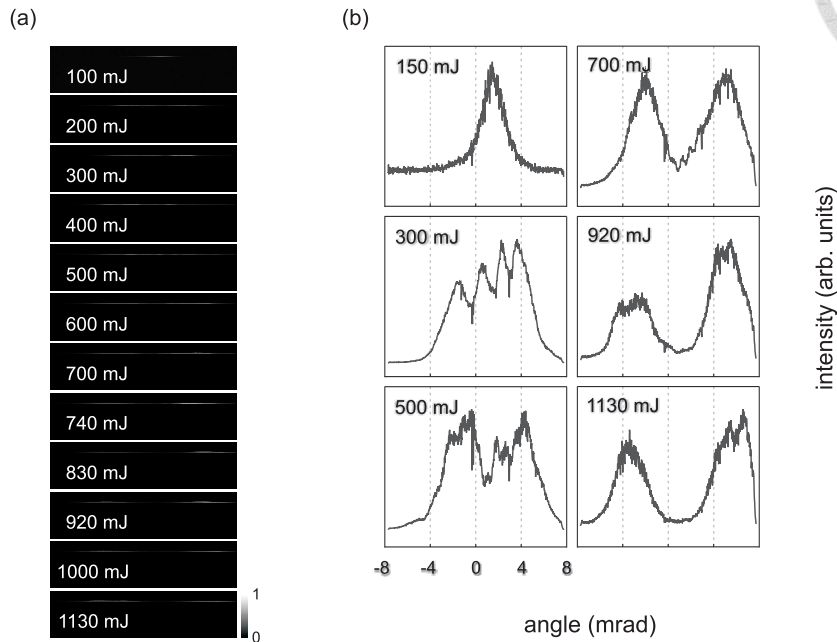
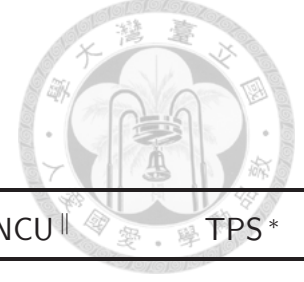


Figure 2.9: (a) Spectral lines of the 32.8-*nm* laser beams for increasing pump pulse energies. (b) Angular distributions of the 32.8-*nm* laser beams for some pump energies corresponding to (a).

the increase of the pump energy results in higher peak intensity which may exceed the ionization threshold of Kr^{9+} and generate an overionization region to reduce the gain volume. Over-ionization took place from the central region outwardly in the channel and may reduce the density barrier of the plasma waveguide by increasing the electron density in the central region. Nonetheless, the transverse intensity distribution of the guided pump pulse also further ionized the outer region of the waveguide to increase the electron density barrier which maintained the guiding condition. The interferometry and relayed imaging system showed that the guiding of the pump pulse in the channel was sufficiently good and the waveguide structure was also sustained even at high pump energy. The propagation of the amplified EUV laser beam is thus guided by the gain volume which had a depressed gain column in the vicinity of the optical axis to produce an annular EUV laser beam.

2.3 Summary

Our laboratory has continually endeavored to improve the performance of



light source	TLS *	IAMS †	NCU ‥	TPS *
commissioning	1993	2007	2012	2014
apparatus	synchrotron	tabletop	tabletop	synchrotron
mechanism	bremsstrahlung	ASE ††	ASE	bremsstrahlung
pulse duration (<i>ps</i>)	100	5 [28]	5	19 [44]
repetition rate (<i>Hz</i>)	$\approx 10^6$	10	10	$\approx 10^6$
wavelength (<i>nm</i>)	tunable	32.8	32.8	tunable
peak spectral brightness ¶ at 32.8 <i>nm</i>	7.9×10^{14} [32]	7.9×10^{23} [45]	1.2×10^{25} [5]	5×10^{18} § [46]

* TL(P)S: Taiwan Light(Photon) Source

† IAMS: Institute of Atomic and Molecular Sciences, Academia Sinica

‡ NCU: National Central University

†† ASE: amplified spontaneous emission

¶ spectral brightness: photons/sec/mm²/mrad² in 0.1% bandwidth

§ EPU100 beamline of Taiwan Photon Source

Table 2.1: Comparison of the EUV laser in this work with that in the previous work and the synchrotron radiations in Taiwan.

EUV lasers these years, fabricating optically preformed plasma waveguides with axicon ignitor-heater scheme [4, 40], seeding of high harmonic generation [43] and characterizing the polarization state and coherence property [32] are some efforts we made in this field.

In this thesis, we observe dramatic enhancement of collisionally excited EUV lasing in optical-field-ionized Ni-like krypton plasmas at 32.8 *nm*. Experimental data revealing the pump energy dependence of the EUV outputs suggests that the lasing is near saturation. At pump energy of 600 *mJ*, the spectral brightness reaches 1.2×10^{25} photons/sec/mm²/mrad² in 0.1% bandwidth. Table 2.1 shows the comparison of our EUV laser with that in the previous work and with the synchrotron radiations of Taiwan's National Synchrotron Radiation Research Center.

On grounds of the introduction of the optically-preformed plasma waveg-



2.3. SUMMARY

uide technique, not only the spectral brightness of the EUV radiation is significantly enhanced, but also the corresponding energy conversion efficiency is raised to an unprecedented level. For comparison, we review some representative achievements here. By virtue of precise pressure control in a capillary waveguide, conversion efficiencies of greater than 10^{-6} at 30 nm were obtained [47]. Similar efficiencies were observed in grazing-incidence pumped transient collisional EUV lasing at 32.6 nm [48], 13.9-nm laser excited by a slab-pumped Ti:sapphire laser [49] and 32.8-nm laser adopting optically preformed plasma waveguide technique [4]. Energy yields of higher-order harmonic radiations in the spectral range of $31\text{--}17\text{ nm}$ were measured up to several tens of nJ , corresponding to conversion efficiencies of as high as 10^{-7} in each harmonic [50]. As the harmonic approaches the regime with higher photon energies, say $\sim 10\text{ nm}$, only a small fraction of pump energy as low as $10^{-11} - 10^{-8}$ could be converted into x-ray photons [51, 52, 53, 54]. In this work, the pulse energy of 32.8-nm EUV lasing pumped by a 100-TW laser system in an optically preformed plasma waveguide reaches $6\ \mu J$ at an energy conversion efficiency of around 10^{-5} [5].

CHAPTER 2. EXTREME-ULTRAVIOLET LASER





Chapter 3

Holographic Processes

A lensless imaging process which is now known as holography was proposed in 1948 by Dennis Gabor to improve the resolution in electron microscopy [55]. Gabor found that the information about both the amplitude and phase of the waves diffracted or scattered from an object can be fully recorded when a coherent reference wave exists simultaneously, which totally contradicts the conventional dogma of optical recording as simple intensity measurement of optical radiations can only store the information of the amplitude distribution the object carries. In holography, the phase information of the object wave buried in a coded form, an interference pattern or simply named a hologram, can ultimately be used to acquire the image of the original object. We review the basic principles behind holographic processes in this chapter and discuss the inherent conundrum of phase ambiguity to be tackled in the next chapters.

3.1 Amplitude and Phase Recording

All the recording media, either chemical or digital, respond only to the light intensity that impinges on it. For that reason, we need the phase information carried by the object wave to somehow be converted into intensity variations for recording purposes. Interferometry is an ingenious thought on that implementation. Think of a reference wave of known amplitude and phase is interfering with the original object wave of unknown wavefront on the recording medium, as shown in Figure 3.1. Note that the wavefront of the reference wave is not necessarily plane, wavefronts of arbitrary shape will do as long as they are mutually coherent with the object field. If complex amplitude of this reference wave is described as

$$E_R(x, y) = a_R(x, y) \exp [j\psi_R(x, y)] \quad (3.1)$$

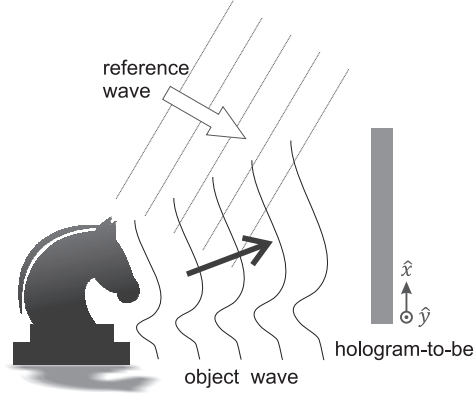


Figure 3.1: Holographic recording*.

with real amplitude a_R and phase ψ_R , while the object wave to be reconstructed is written as

$$E_O(x, y) = a_O(x, y) \exp [j\psi_O(x, y)] \quad (3.2)$$

with real amplitude a_O and phase ψ_O . The intensity of the interfering field of two complex waves is thus

$$\begin{aligned} I(x, y) &= |E_O(x, y) + E_R(x, y)|^2 \\ &= E_O(x, y)E_O^*(x, y) + E_R(x, y)E_R^*(x, y) \\ &\quad + E_O(x, y)E_R^*(x, y) + E_R(x, y)E_O^*(x, y) \\ &= a_O^2(x, y) + a_R^2(x, y) \\ &\quad + 2a_O(x, y)a_R(x, y) \cos [\psi_O(x, y) - \psi_R(x, y)]. \end{aligned} \quad (3.3)$$

The first two terms of Eq.(3.3) contain no information about the object phase at all. It is the third term that codes the phase information in a decipherable way to be retrieved during the holographic reconstruction. Now, the question remains is how we reconstruct the object wave $E_O(x, y)$ given the interferometric recording.

3.2 Wavefront Reconstruction

The interference pattern from the variations of exposure on the recording medium is assumed to be processed so that its amplitude transmittance t_A depends linearly on the interferometric intensity [56, 57, 58]

$$t_A(x, y) = t_0 + \beta\tau I(x, y), \quad (3.4)$$

3.2. WAVEFRONT RECONSTRUCTION

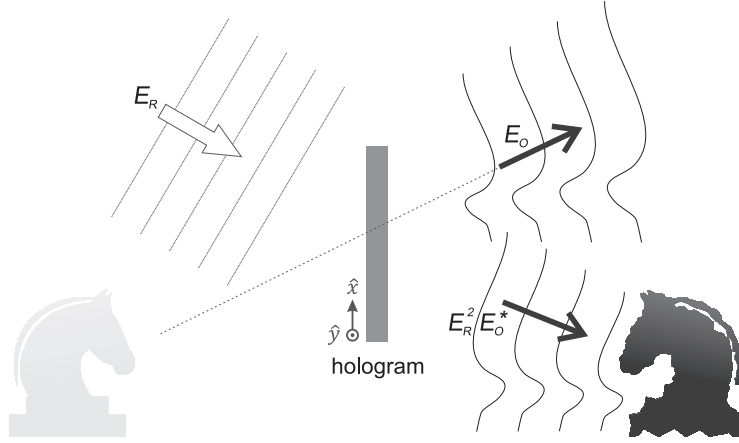


Figure 3.2: Holographic reconstruction via illumination of the original reference wave. The real image of the object is distorted by E_R^2 .

where t_0 is the constant background transmittance, β is the slope of the amplitude transmittance versus exposure characteristic of the recording medium and τ is the exposure time. Assume that we illuminate a transparency possessing the amplitude transmittance of the form Eq.(3.4) with the aforementioned reference wave $E_R(x, y)$, now acting as the reconstruction wave. The wave field transmitted through the transparency is

$$E_R(x, y) t_A(x, y) = \left\{ t_0 + \beta\tau [a_O^2(x, y) + a_R^2(x, y)] \right\} E_R(x, y) + \beta\tau a_R^2(x, y) E_O(x, y) + \beta\tau E_R^2(x, y) E_O^*(x, y). \quad (3.5)$$

The first term on the right-hand side of the equation is the scaled reference wave, representing the zeroth-order undiffracted wave directly passing through the hologram. The reconstructed wavefront $\beta\tau a_R^2(x, y) E_O(x, y)$ is, up to a $\beta\tau a_R^2(x, y)$ that only influences the brightness of the image, clearly a duplication of the original object wave. The last term generates a distorted real image of the object, whose distortion comes from the spatially varying complex factor $E_R^2(x, y)$ that modulates conjugate object wave $E_O^*(x, y)$ as illustrated in Figure 3.2. If an undistorted real object image is desired, the conjugate reference beam could be employed for reconstruction, like that shown in Figure 3.3,

$$E_R^*(x, y) t_A(x, y) = \left\{ t_0 + \beta\tau [a_O^2(x, y) + a_R^2(x, y)] \right\} E_R^*(x, y) + \beta\tau a_R^2(x, y) E_O^*(x, y) + \beta\tau E_R^{*2}(x, y) E_O(x, y). \quad (3.6)$$

The second term of the above equation serves the need for the original object appearance.

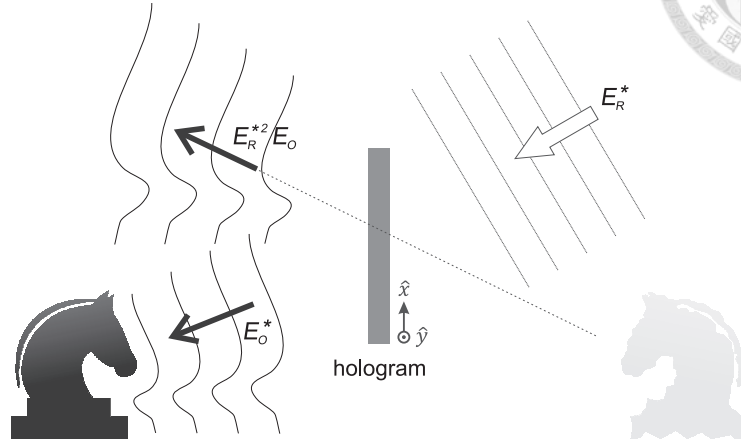


Figure 3.3: Holographic reconstruction via illumination of the conjugate reference wave. The real image of the object is undistorted while the virtual image is distorted by E_R^{*2} .

3.3 Twin Images

When the reconstruction and the reference waves are from the same side of the hologram, similar to the case depicted in Figure 3.2, the holographic term $\beta\tau a_R^2(x, y)E_O(x, y)$ appearing in Eq.(3.5) forms a virtual image on the same side as the object, but the opposite side of the real image from the term $\beta\tau E_R^2(x, y)E_O^*(x, y)$. These two terms constitute a pair of twin images with respect to each other, and this fact really stirs the pot when it comes to taking clear images. Suppose that the observation plane is now taken to be on the real image, the wave field from the virtual image propagates to and deposits on this plane obscures the real image, largely compromising the image quality. Even if Figure 3.3 is now considered, the reconstruction and the reference waves are from the opposite side of the hologram, image obscuration still cannot be weeded out. The existence of twin image is an inherent and unavoidable problem in holography.

3.4 Holographic Microscopy

At a given focal position of a conventional microscope, the micrograph inside the field of view consists of the image plane in sharp focus together with the blurred background coming from the out-of-focus planes of the extended object. The information of all the out-of-focus volume buried in the blurred background is literally wasted from the perspective of thorough recording for truthful imaging. With an even higher magnification, the severer decreasing



3.4. HOLOGRAPHIC MICROSCOPY

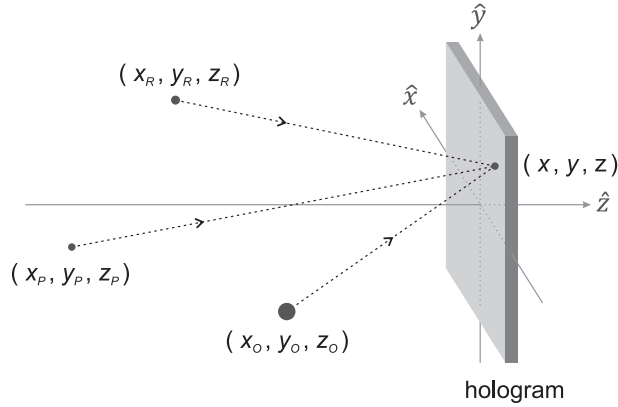


Figure 3.4: Holographic recording and reconstruction geometries.

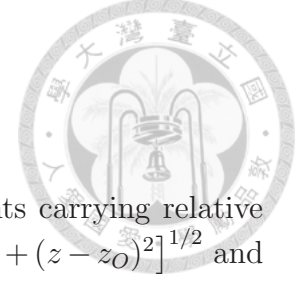
depth of field limits the observed field of conventional microscopy to an even narrower slice, leaving more region-to-be-inspected unknown. On the contrary, holographic microscopy is capable of recording the entire volume of an extended object on a single hologram through the interferometric technique brought up in the preceding sections [59, 60].

3.4.1 Image Positions and Magnification

It is convenient to consider the hologram made from a point object located at (x_O, y_O, z_O) , interfered by and recorded with a reference wave from a point source at (x_R, y_R, z_R) . After the interference is recorded, a spherical wave emitting from a point source at (x_P, y_P, z_P) plays the role of the reconstruction wave to illuminate the developed hologram. The sign convention adopted here in the analysis follows Goodman's suggestion that all z_O and z_R and z_P are assigned negative values for point sources lying to the left of the hologram [56]. The holographic processing geometry is illustrated in Figure 3.4.

The intensity distribution falling on the recording medium is from the interference pattern between the object and the reference spherical divergent waves,

$$I(x, y) = \left| \frac{a_O}{r_O} \exp \left[j \frac{2\pi}{\lambda_O} \sqrt{(x - x_O)^2 + (y - y_O)^2 + (z - z_O)^2} \right] + \frac{a_R}{r_R} \exp \left[j \frac{2\pi}{\lambda_R} \sqrt{(x - x_R)^2 + (y - y_R)^2 + (z - z_R)^2} \right] \right|^2, \quad (3.7)$$



where a_O/r_O and a_R/r_R are complex amplitude constants carrying relative phases of the two waves with $r_O = [(x - x_O)^2 + (y - y_O)^2 + (z - z_O)^2]^{1/2}$ and $r_R = [(x - x_R)^2 + (y - y_R)^2 + (z - z_R)^2]^{1/2}$. Under the paraxial approximation, Eq.(3.7) can be approximated to

$$\begin{aligned}
 I(x, y) &= \left| \frac{a_O}{r_O} \right|^2 + \left| \frac{a_R}{r_R} \right|^2 \\
 &+ \left(\frac{a_O}{r_O} \right) \left(\frac{a_R}{r_R} \right)^* \exp \left\{ j \frac{2\pi}{\lambda_O} \sqrt{(x - x_O)^2 + (y - y_O)^2 + (z - z_O)^2} \right. \\
 &\quad \left. - j \frac{2\pi}{\lambda_R} \sqrt{(x - x_R)^2 + (y - y_R)^2 + (z - z_R)^2} \right\} \\
 &+ \left(\frac{a_O}{r_O} \right)^* \left(\frac{a_R}{r_R} \right) \exp \left\{ -j \frac{2\pi}{\lambda_O} \sqrt{(x - x_O)^2 + (y - y_O)^2 + (z - z_O)^2} \right. \\
 &\quad \left. + j \frac{2\pi}{\lambda_R} \sqrt{(x - x_R)^2 + (y - y_R)^2 + (z - z_R)^2} \right\} \\
 &\approx \left| \frac{a_O}{z - z_O} \right|^2 + \left| \frac{a_R}{z - z_R} \right|^2 \\
 &+ \left(\frac{a_O}{z - z_O} \right) \left(\frac{a_R}{z - z_R} \right)^* \exp \left[j 2\pi \left(\frac{z - z_O}{\lambda_O} - \frac{z - z_R}{\lambda_R} \right) \right] \\
 &\quad \cdot \exp \left\{ j \frac{\pi}{\lambda_O(z - z_O)} \left[(x - x_O)^2 + (y - y_O)^2 \right] \right. \\
 &\quad \left. - j \frac{\pi}{\lambda_R(z - z_R)} \left[(x - x_R)^2 + (y - y_R)^2 \right] \right\} \\
 &+ \left(\frac{a_O}{z - z_O} \right)^* \left(\frac{a_R}{z - z_R} \right) \exp \left[j 2\pi \left(\frac{z - z_R}{\lambda_R} - \frac{z - z_O}{\lambda_O} \right) \right] \\
 &\quad \cdot \exp \left\{ -j \frac{\pi}{\lambda_O(z - z_O)} \left[(x - x_O)^2 + (y - y_O)^2 \right] \right. \\
 &\quad \left. + j \frac{\pi}{\lambda_R(z - z_R)} \left[(x - x_R)^2 + (y - y_R)^2 \right] \right\}. \quad (3.8)
 \end{aligned}$$

If Eq.(3.4) still holds, the last two terms of Eq.(3.8) contribute to two (x, y) -dependent transmitting amplitudes of the developed hologram when illumi-

3.4. HOLOGRAPHIC MICROSCOPY



nated by a paraxial spherical reconstruction wave of the form

$$E_P(x, y) \approx \left(\frac{a_P}{z - z_P} \right) \exp \left[j2\pi \left(\frac{z - z_P}{\lambda_P} \right) \right] \cdot \exp \left\{ j \frac{\pi}{\lambda_P (z - z_P)} \left[(x - x_P)^2 + (y - y_P)^2 \right] \right\}. \quad (3.9)$$

To simplify the derivation, we put the hologram at $z = 0$ and neglect all the coefficients that are (x, y) -independent. The twin transmitting waves thus take the forms of

$$E_T(x, y) = \beta\tau E_P(x, y) \left[I(x, y) - \left| \frac{a_O}{r_O} \right|^2 - \left| \frac{a_R}{r_R} \right|^2 \right] \propto \exp \left\{ -j \frac{\pi}{\lambda_P z_P} \left[(x - x_P)^2 + (y - y_P)^2 \right] \mp j \frac{\pi}{\lambda_O z_O} \left[(x - x_O)^2 + (y - y_O)^2 \right] \pm j \frac{\pi}{\lambda_R z_R} \left[(x - x_R)^2 + (y - y_R)^2 \right] \right\} \quad (3.10)$$

$$= \exp \left\{ -j \frac{\pi}{\lambda_P z_T} \left[(x - x_T)^2 + (y - y_T)^2 \right] \right\}. \quad (3.11)$$

It is readily to obtain the location of the image point (x_T, y_T, z_T) through direct term-by-term comparisons of Eq.(3.10) and Eq.(3.11), which gives

$$\left(\text{pickup of } x^2 \text{ or } y^2 \right) \quad \frac{-1}{\lambda_P z_T} = \frac{-1}{\lambda_P z_P} \mp \frac{1}{\lambda_O z_O} \pm \frac{1}{\lambda_R z_R} \quad (3.12)$$

$$\left(\text{pickup of linear terms in } x \right) \quad \frac{x_T}{\lambda_P z_T} = \frac{x_P}{\lambda_P z_P} \pm \frac{x_O}{\lambda_O z_O} \mp \frac{x_R}{\lambda_R z_R} \quad (3.13)$$

$$\left(\text{pickup of linear terms in } y \right) \quad \frac{y_T}{\lambda_P z_T} = \frac{y_P}{\lambda_P z_P} \pm \frac{y_O}{\lambda_O z_O} \mp \frac{y_R}{\lambda_R z_R}. \quad (3.14)$$

Intuitively, an extended object can be thought of as being composed of many point objects whose behaviors are dictated by the theory from the above analysis. By virtue of locating every image point of the extended object, the eventual delineation determines the transverse and longitudinal



magnifications. From Eq.(3.13) and Eq.(3.14), the transverse magnification M_t is derived as

$$\begin{aligned} M_t \equiv \frac{\partial x_T}{\partial x_O} = \frac{\partial y_T}{\partial y_O} &= \frac{\pm 1}{\lambda_O z_O} \left(\frac{1}{\lambda_P z_P} \pm \frac{1}{\lambda_O z_O} \mp \frac{1}{\lambda_R z_R} \right)^{-1} \\ &= \left(\pm \frac{\lambda_O z_O}{\lambda_P z_P} + 1 - \frac{\lambda_O z_O}{\lambda_R z_R} \right)^{-1}, \end{aligned} \quad (3.15)$$

while Eq.(3.12) and Eq.(3.15) help to deduce the longitudinal magnification M_ℓ that is given by

$$\begin{aligned} M_\ell \equiv \frac{\partial z_T}{\partial z_O} &= \pm \frac{\lambda_P}{\lambda_O} \left(\frac{z_T}{z_O} \right)^2 = \pm \frac{\lambda_P}{\lambda_O} \left(\frac{z_O}{z_P} \pm \frac{\lambda_p}{\lambda_O} \mp \frac{\lambda_p z_O}{\lambda_R z_R} \right)^{-2} \\ &= \pm \frac{\lambda_P}{\lambda_O} \left(\frac{\lambda_O}{\lambda_P} \right)^2 \left(\pm \frac{\lambda_O z_O}{\lambda_P z_P} + 1 - \frac{\lambda_O z_O}{\lambda_R z_R} \right)^{-2} \\ &= \pm \frac{\lambda_O}{\lambda_P} M_t^2. \end{aligned} \quad (3.16)$$

The opposite signs in Eq.(3.16) implies that the two conjugate images exhibit distinct parallax perspectives, a sensation to tell front from rear, far from near or deep from shallow.

3.4.2 Equivalence of Gabor and Fourier Holography

A simplified layout of in-line Fourier holography is illustrated in Figure 3.5 (a). Assume that an ideal point source $\delta(\mathbf{r}_0)$ serves as the light source to irradiate the object with a transmission function $T(\mathbf{r}_1)$ at $z = z_1$ and the diffraction pattern is recorded by a detector at plane $z = z_2$, where $\mathbf{r}_m \equiv (x_m, y_m)$ are two-dimensional rectangular spatial coordinates with $m = \{0, 1, 2\}$. According to the Huygens-Fresnel principle under the paraxial approximation [56], the spherical incident wave $U_1(\mathbf{r}_1)$ that illuminates the object is given by

$$\begin{aligned} U_1(\mathbf{r}_1) &= \frac{e^{jkz_{10}}}{j\lambda z_{10}} \iint_{-\infty}^{\infty} \delta(\mathbf{r}_0) \exp \left[j \frac{k}{2z_{10}} (\mathbf{r}_1 - \mathbf{r}_0)^2 \right] d\mathbf{r}_0 \\ &= \frac{e^{jkz_{10}}}{j\lambda z_{10}} \exp \left(j \frac{k}{2z_{10}} \mathbf{r}_1^2 \right), \end{aligned} \quad (3.17)$$

where k is the wavenumber, λ is the wavelength of the light source and $z_{10} = z_1 - z_0$ is the distance from source to object. After transmitting through



3.4. HOLOGRAPHIC MICROSCOPY

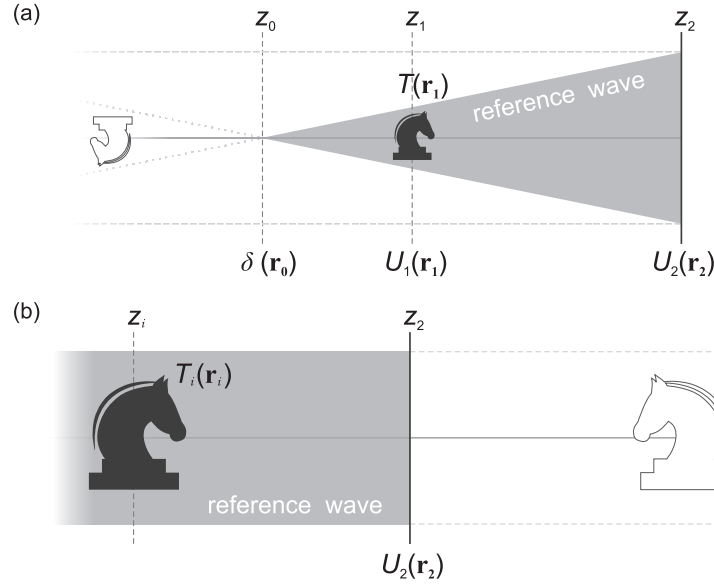


Figure 3.5: Two equivalent holographic recording schemes: (a) Fourier type with a spherical reference beam and (b) Gabor type with a planar reference wave. The black knights are the objects while the white knights stand for the corresponding twin images.

the object, the unscattered reference wave and the scattered object wave travel to the detector and interfere with each other to form the hologram. The total field distribution on the detector can be expressed as

$$\begin{aligned}
 U_2(\mathbf{r}_2) &= \frac{e^{jkz_{21}}}{j\lambda z_{21}} \iint_{-\infty}^{\infty} U_1(\mathbf{r}_1) T(\mathbf{r}_1) \exp \left[j \frac{k}{2 z_{21}} (\mathbf{r}_2 - \mathbf{r}_1)^2 \right] d\mathbf{r}_1 \\
 &= \frac{-e^{jkz_{20}}}{\lambda^2 z_{21} z_{10}} \exp \left(j \frac{k}{2 z_{21}} \mathbf{r}_2^2 \right) \iint_{-\infty}^{\infty} T(\mathbf{r}_1) \\
 &\quad \cdot \exp \left[j \frac{k}{2} \underbrace{\left(\frac{1}{z_{10}} + \frac{1}{z_{21}} \right)}_{=M/z_{21}} \mathbf{r}_1^2 \right] \exp \left(-j \frac{k \mathbf{r}_1 \cdot \mathbf{r}_2}{z_{21}} \right) d\mathbf{r}_1 \\
 &= \frac{-e^{jkz_{20}}}{\lambda^2 z_{21} z_{10}} \exp \left[j \frac{k}{2} \left(\frac{1}{z_{20}} + \frac{1}{M z_{21}} \right) \mathbf{r}_2^2 \right] \iint_{-\infty}^{\infty} T(\mathbf{r}_1) \\
 &\quad \cdot \exp \left(j \frac{M^2 k}{2 M z_{21}} \mathbf{r}_1^2 \right) \exp \left(-j \frac{M k \mathbf{r}_1 \cdot \mathbf{r}_2}{M z_{21}} \right) d\mathbf{r}_1
 \end{aligned}$$



$$\begin{aligned}
 &= \frac{-e^{jkz_{20}}}{\lambda^2 z_{21} z_{10}} \exp\left(j \frac{k}{2 z_{20}} \mathbf{r}_2^2\right) \\
 &\quad \cdot \iint_{-\infty}^{\infty} T(\mathbf{r}_1) \exp\left[j \frac{k}{2 M z_{21}} (\mathbf{r}_2 - M \mathbf{r}_1)^2\right] d\mathbf{r}_1, \quad (3.18)
 \end{aligned}$$

where $z_{20} = z_2 - z_0$, $z_{21} = z_2 - z_1$ and $M = z_{20}/z_{10}$ denotes the geometric magnification. In optical imaging, an M -times enlarged image is related to its object by $T_i(\mathbf{r}_i) = T(\mathbf{r}_i/M)/|M|$. By selecting $\mathbf{r}_i = M \mathbf{r}_1$, Eq.(3.18) can be rearranged in the form of

$$\begin{aligned}
 U_2(\mathbf{r}_2) &= \frac{-e^{jkz_{20}}}{\lambda^2 z_{21} z_{10}} \exp\left(j \frac{k}{2 z_{20}} \mathbf{r}_2^2\right) \\
 &\quad \cdot \iint_{-\infty}^{\infty} T_i(\mathbf{r}_i) \exp\left[j \frac{k}{2 M z_{21}} (\mathbf{r}_2 - \mathbf{r}_i)^2\right] d\mathbf{r}_i. \quad (3.19)
 \end{aligned}$$

Except for the quadratic phase term, the field $U_2(\mathbf{r}_2)$ in Eq.(3.19) has the same form as that of the interference pattern produced by illuminating an M -times magnified object with a planar reference wave and placing the detector at $M z_{21}$ downstream of the object as shown in Figure 3.5 (b), where $z_i = z_2 - M z_{21}$. Since the moduli of the interference patterns observed in both holographic schemes are identical, Fourier holography can be equivalently transformed into a Gabor's configuration deployed for a magnified object and the solution to the twin image problem can also be applied on both schemes.



Chapter 4

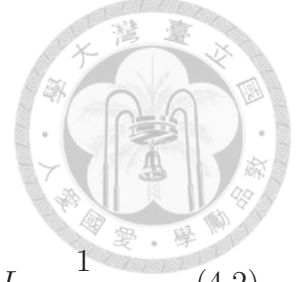
Digital Holography

Replacing photochemical recording media with electronic sensors and propagating complex electromagnetic waves numerically, digital holography as a burgeoning field in holographic imaging is capable of acquiring and processing the holograms at faster speeds. By virtue of numerically focusing on the different layers of an extended object, this computerized technology is able to collect the information of three-dimensional structure without adjusting the mechanical setup for implementing optical scanning through the region with different depths. Furthermore, what seems totally infeasible in conventional holography but now viable in digital holography lies in an advantage that quantitative phase distributions on any plane can be easily retrieved and displayed on the monitor of your personal computer. To enjoy all those merits the digital technique brings, comprehending the basic principles behind it is the first step.

4.1 Discrete Fourier Transform

Let's begin with a continuous function $f(t)$ and its Fourier transform $\mathcal{F}f(s)$. We want to know how the discrete version of $\mathcal{F}f(s)$ is related to the discrete version of $f(t)$. Suppose that $f(t)$ is only nonzero inside of $0 \leq t \leq L$ and $\mathcal{F}f(s)$ is effectively zero outside of $0 < s < 2B$. Without loss of generality, both L and B are taken to be integers. According to the Shannon Sampling Theorem, $f(t)$ can be perfectly reconstructed from its samples if the sampling rate is not less than the signal's Nyquist frequency, $2B$ in this case. If we sample $f(t)$ at Nyquist frequency, a total of

$$N = \frac{L}{1/(2B)} = 2BL \quad (4.1)$$



samples are obtained at evenly spaced points

$$t_0 = 0, \quad t_1 = \frac{1}{2B}, \quad t_2 = \frac{2}{2B}, \quad \dots, \quad t_{N-1} = \frac{N-1}{2B} = L - \frac{1}{2B}. \quad (4.2)$$

The discrete version of $f(t)$, referred to as $f_d(t)$, is therefore the sequence of sampled points $f(t_0), f(t_1), f(t_2), \dots, f(t_{N-1})$. With the help of the shah function [61],

$$f_d(t) = f(t) \sum_{k=0}^{N-1} \delta(t - t_k) = \sum_{k=0}^{N-1} f(t_k) \delta(t - t_k), \quad (4.3)$$

where $\delta(t)$ represents the Dirac delta function. The Fourier transform of $f_d(t)$ is

$$\mathcal{F}f_d(s) = \sum_{k=0}^{N-1} f(t_k) \mathcal{F}\delta(t - t_k) = \sum_{k=0}^{N-1} f(t_k) e^{-2\pi i s t_k}. \quad (4.4)$$

Next we try to discretize $\mathcal{F}f_d(s)$ in a similar way mentioned above, that is, $\mathcal{F}f_d(s)$ must be sampled over the interval $0 < s < 2B$ in the frequency domain at points evenly spaced $1/L$ apart as

$$s_0 = 0, \quad s_1 = \frac{1}{L}, \quad s_2 = \frac{2}{L}, \quad \dots, \quad s_{N-1} = \frac{N-1}{L} = 2B - \frac{1}{L}. \quad (4.5)$$

The discrete version of $\mathcal{F}f_d(s)$ can accordingly be expressed as

$$\begin{aligned} F(s_0) &= \sum_{k=0}^{N-1} f(t_k) e^{-2\pi i s_0 t_k}, \\ F(s_1) &= \sum_{k=0}^{N-1} f(t_k) e^{-2\pi i s_1 t_k}, \\ &\vdots \\ F(s_{N-1}) &= \sum_{k=0}^{N-1} f(t_k) e^{-2\pi i s_{N-1} t_k}. \end{aligned} \quad (4.6)$$

From Eqs.(4.1) (4.2) (4.5) (4.6), we are now in a position to write down the definition of the discrete version of the Fourier transform of the discrete version of a continuous function. Here is the terse version of its mathematical description. Given the sample points in both domains

$$t_k = \frac{k}{2B}, \quad s_m = \frac{m}{L}, \quad (4.7)$$

4.1. DISCRETE FOURIER TRANSFORM



we obtain

$$F(s_m) = \sum_{k=0}^{N-1} f(t_k) e^{-2\pi i s_m t_k} = \sum_{k=0}^{N-1} f(t_k) e^{-2\pi i m k / N}. \quad (4.8)$$

But what if the original signal is born discrete rather than from sampling? Consider an operation that maps an ordered sequence of N numbers into another ordered sequence of N numbers. The ordered sequences here can be deemed two sequential samplings as those discussed above, and their mapping by design is subjected to the operation that implements Eq.(4.8). If an ordered sequence of N elements is expressed as an N -tuple vector as $\mathbf{f} = (\mathbf{f}[0], \mathbf{f}[1], \mathbf{f}[2], \dots, \mathbf{f}[N-1])$, the discrete Fourier transform of \mathbf{f} can be unhesitatingly written as

$$\mathbb{F}[m] = \sum_{k=0}^{N-1} \mathbf{f}[k] e^{-2\pi i m k / N}, \quad m = 0, 1, 2, \dots, N-1. \quad (4.9)$$

Due to the immanent symmetry existing between the formalisms of Fourier transform and its inverse counterpart [62], the inverse discrete Fourier transform $\tilde{\mathbb{F}}^{-1}$ is supposed to take the form of

$$\mathbf{f}[k] = \frac{1}{\square} \sum_{m=0}^{N-1} \mathbb{F}[m] e^{2\pi i m k / N}, \quad k = 0, 1, 2, \dots, N-1, \quad (4.10)$$

To determine the constant \square , we resort to the identity $\tilde{\mathbb{F}}^{-1} \tilde{\mathbb{F}} \mathbf{f} = \mathbf{f}$. With this,

$$\begin{aligned} \tilde{\mathbb{F}}^{-1} \tilde{\mathbb{F}} \mathbf{f} &= \tilde{\mathbb{F}}^{-1} \sum_{k=0}^{N-1} \mathbf{f}[k] \cdot \left(1, e^{-2\pi i(1)k/N}, e^{-2\pi i(2)k/N}, \dots, e^{-2\pi i(N-1)k/N} \right) \\ &= \sum_{k=0}^{N-1} \mathbf{f}[k] \tilde{\mathbb{F}}^{-1} \left(1, e^{-2\pi i(1)k/N}, e^{-2\pi i(2)k/N}, \dots, e^{-2\pi i(N-1)k/N} \right) \\ &= \mathbf{f} = \sum_{k=0}^{N-1} \mathbf{f}[k] \boldsymbol{\delta}_k, \end{aligned} \quad (4.11)$$

where $\boldsymbol{\delta}_k = (0, \dots, 0, 1, 0, \dots, 0)$ is the shifted discrete delta vector with unity in the k -th element and zeros elsewhere. Obviously, Eq.(4.11) suggests that



$\tilde{\mathbb{F}}^{-1}(1, e^{-2\pi i(1)k/N}, e^{-2\pi i(2)k/N}, \dots, e^{-2\pi i(N-1)k/N})$ be equal to δ_k , which gives

$$\begin{aligned} \frac{1}{\square} \sum_{m=0}^{N-1} e^{-2\pi i m k / N} \cdot e^{2\pi i m k' / N} &= \frac{1}{\square} \sum_{m=0}^{N-1} e^{-2\pi i m (k-k') / N} = \delta_k[k'] \\ &\xrightarrow{k'=k} \frac{N}{\square} = 1 \quad \therefore \square = N. \end{aligned} \quad (4.12)$$

Up to now, the discussion has been limited to one-dimensional case. With the help of Eqs.(4.9) (4.10) (4.12), two-dimensional discrete Fourier transform pair can be readily extended to

$$\begin{aligned} \mathbb{F}[m, n] &= \sum_{k=0}^{N-1} \sum_{\ell=0}^{Q-1} \mathbf{f}[k, \ell] \exp \left[-2\pi i \left(\frac{mk}{N} + \frac{n\ell}{Q} \right) \right], \\ \mathbf{f}[k, \ell] &= \frac{1}{NQ} \sum_{m=0}^{N-1} \sum_{n=0}^{Q-1} \mathbb{F}[m, n] \exp \left[2\pi i \left(\frac{mk}{N} + \frac{n\ell}{Q} \right) \right], \end{aligned} \quad (4.13)$$

for $m, k = 0, 1, 2, \dots, N - 1$ and $n, \ell = 0, 1, 2, \dots, Q - 1$.

4.2 Numerical Propagation

The basic principle of light wave propagation is reviewed, and the discrete version of diffraction formulae suited for implementing wave propagation on a computer is also introduced in this section. We mainly focus on two numerical methods, and characterize each of them with simulation demonstrations.

4.2.1 Fresnel Transform Method

The Huygens-Fresnel principle can be comprehended in a physical picture that the observed field at some spatial position is a superposition of diverging spherical wavelets emitting from every secondary sources within the aperture which is pervious to light. Under the paraxial approximation, the Huygens-Fresnel principle can be described with the mathematical expression [56]

$$U(x, y) = \frac{e^{jkz}}{j\lambda z} \iint_{-\infty}^{\infty} U(\xi, \eta) \exp \left\{ j \frac{k}{2z} \left[(x - \xi)^2 + (y - \eta)^2 \right] \right\} d\xi d\eta, \quad (4.14)$$



4.2. NUMERICAL PROPAGATION

where (x, y) is the coordinate of diffraction plane, (ξ, η) is the coordinate of source plane, k is the wavenumber and λ is the wavelength of the light source. Expanding the quadratic terms of Eq.(4.14) and then rearranging the whole equation, we get a more suggestive form

$$\begin{aligned} U(x, y) &= \frac{e^{jkz}}{j\lambda z} e^{j\frac{k}{2z}(x^2+y^2)} \iint_{-\infty}^{\infty} \left[U(\xi, \eta) e^{j\frac{k}{2z}(\xi^2+\eta^2)} \right] e^{-j\frac{2\pi}{\lambda z}(x\xi+y\eta)} d\xi d\eta \\ &= \frac{e^{jkz}}{j\lambda z} e^{j\frac{k}{2z}(x^2+y^2)} \mathcal{F} \left\{ U(\xi, \eta) e^{j\frac{k}{2z}(\xi^2+\eta^2)} \right\} \left[\frac{x}{\lambda z}, \frac{y}{\lambda z} \right]. \end{aligned} \quad (4.15)$$

To make $U(x, y)$ computable on a machine, we transform Eq.(4.15) into its discrete version

$$\begin{aligned} \mathbb{U}[m, n] &= \frac{e^{jkz}}{j\lambda z} e^{j\frac{k}{2z}(m^2\Delta x^2+n^2\Delta y^2)} \\ &\quad \cdot \sum_{k=0}^{N-1} \sum_{\ell=0}^{Q-1} \left\{ \mathbb{U}[k, \ell] e^{j\frac{k}{2z}(k^2\Delta\xi^2+\ell^2\Delta\eta^2)} \right\} e^{-j\frac{2\pi}{\lambda z}(mk\Delta x\Delta\xi+n\ell\Delta y\Delta\eta)} \\ &= \frac{e^{jkz}}{j\lambda z} e^{j\frac{k}{2z}(m^2\Delta x^2+n^2\Delta y^2)} \tilde{\mathbb{F}} \left\{ \mathbb{U}[k, \ell] e^{j\frac{k}{2z}(k^2\Delta\xi^2+\ell^2\Delta\eta^2)} \right\} [m, n]. \end{aligned} \quad (4.16)$$

Apparently from its appearance, a discrete Fourier transform is involved in the computation with the two domains being discretized in pixel sizes $\Delta x \times \Delta y$ and $\Delta\xi \times \Delta\eta$ respectively.

An opaque letter 'R' in a transparent screen of $512 \times 512 \mu m^2$ with $1,023 \times 1,023$ pixels is located at $z = 0$ and numerically illuminated by a plane wave with $\lambda = 632.8 \text{ nm}$. Figure 4.1(a) shows the amplitude distributions of the diffracted fields at distances $z = 0, 100, 200, 300 \mu m$ while (b) shows their corresponding phase maps. It is clear that the field of view increases with the diffraction distance as the pixel sizes at different positions are not constant. According to the sampling theory, the sampling interval in the spatial domain determines the maximum frequency in a fashion of

$$\begin{aligned} f_{max} = N\Delta f = \frac{1}{\Delta\xi} &\implies N\Delta\left(\frac{x}{\lambda z}\right) = \frac{1}{\Delta\xi} \\ &\implies \Delta x = \frac{\lambda z}{N\Delta\xi}. \end{aligned} \quad (4.17)$$

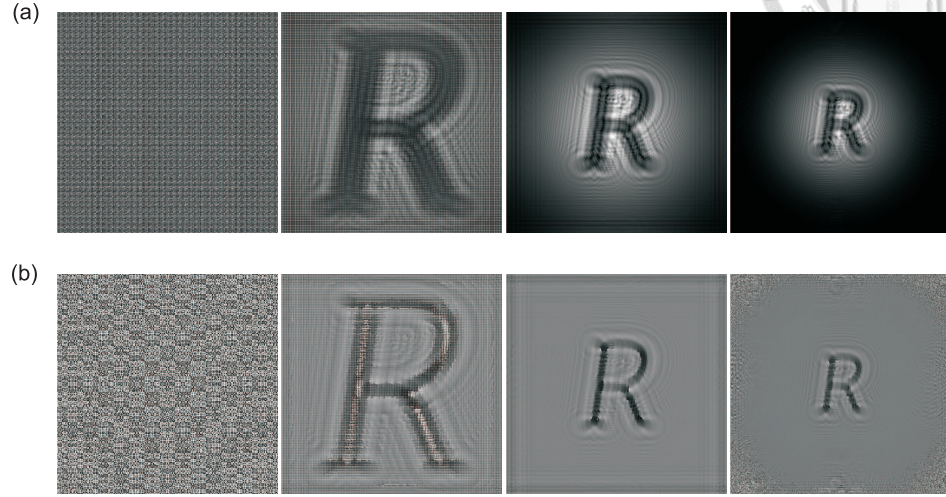
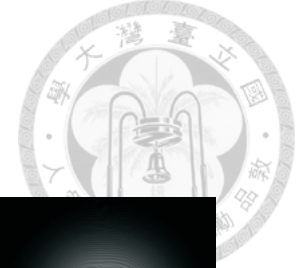


Figure 4.1: (a) Amplitude and (b) phase maps of the numerical diffractions with Fresnel transform method at $z = 0, 100, 200, 300 \mu m$.

As it discloses, the pixel size Δx in the spatial domain scales with the propagation distance z , leading to the broadening fields of view like those shown in Figure 4.1. At $z = 0, 100, 200, 300 \mu m$, the fields of view are $0, 127 \times 127, 253 \times 253, 380 \times 380 \mu m^2$ correspondingly.

Variation in pixel size is definitely no good in volumetric imaging. To neutralize such adversity, we need a sounder solution.

4.2.2 Fresnel Convolution Method

Introducing the Fresnel kernel [56, 63]

$$h(x, y) = \frac{e^{jkz}}{j\lambda z} \exp \left[j \frac{k}{2z} (x^2 + y^2) \right], \quad (4.18)$$

Eq.(4.14) is nothing but a convolution of the form

$$U(x, y) = \iint_{-\infty}^{\infty} U(\xi, \eta) h(x - \xi, y - \eta) d\xi d\eta. \quad (4.19)$$



We Fourier transform the kernel so as to derive the diffraction transfer function

$$\begin{aligned}
H(f_X, f_Y) &= \frac{e^{jkz}}{j\lambda z} \mathcal{F} \left\{ \exp \left[j \frac{\pi}{\lambda z} (x^2 + y^2) \right] \right\} \\
&= \frac{e^{jkz}}{j\lambda z} \mathcal{F} \left\{ \exp \left[-\pi \left(\sqrt{\frac{-j}{\lambda z}} x \right)^2 - \pi \left(\sqrt{\frac{-j}{\lambda z}} y \right)^2 \right] \right\} \\
&= \frac{e^{jkz}}{j\lambda z \sqrt{\frac{-j}{\lambda z}} \sqrt{\frac{-j}{\lambda z}}} \exp \left[-\pi \left(\frac{f_X^2}{\sqrt{\frac{-j}{\lambda z}}^2} + \frac{f_Y^2}{\sqrt{\frac{-j}{\lambda z}}^2} \right) \right] \\
&= e^{jkz} \exp \left[-j\pi\lambda z \left(f_X^2 + f_Y^2 \right) \right]. \tag{4.20}
\end{aligned}$$

Now, Eq.(4.19) can be rewritten as

$$\begin{aligned}
U(x, y) &= \mathcal{F}^{-1} \mathcal{F} \{ U(x, y) \} \\
&= \mathcal{F}^{-1} \mathcal{F} \left\{ \iint_{-\infty}^{\infty} U(\xi, \eta) h(x - \xi, y - \eta) d\xi d\eta \right\} \\
&= \mathcal{F}^{-1} \left\{ \mathcal{F}U[f_X, f_Y] \cdot H(f_X, f_Y) \right\}. \tag{4.21}
\end{aligned}$$

For numerical computation as usual, we transform the above equation into its discrete version

$$\begin{aligned}
\mathbf{U}[k, \ell] &= \tilde{\mathbb{F}}^{-1} \left\{ \tilde{\mathbb{F}} \mathbf{U}[m, n] \cdot \mathbb{H}[m, n] \right\} \\
&= \tilde{\mathbb{F}}^{-1} \left\{ \tilde{\mathbb{F}} \mathbf{U}[m, n] \cdot e^{jkz} \exp \left[-j\pi\lambda z \left(m^2 \Delta x^2 + n^2 \Delta y^2 \right) \right] \right\}. \tag{4.22}
\end{aligned}$$

Similarly, the maximum frequency is determined by the sampling interval in the spatial domain

$$f_{max} = N\Delta x = \frac{1}{\Delta\xi} \implies \Delta x = \frac{1}{N\Delta\xi}. \tag{4.23}$$

The simulation example adopting the same set of parameters as that shown in 4.2.1 is demonstrated here with the Fresnel convolution method, whose results are listed in Figure 4.2. Unlike the previous results, the pixel size

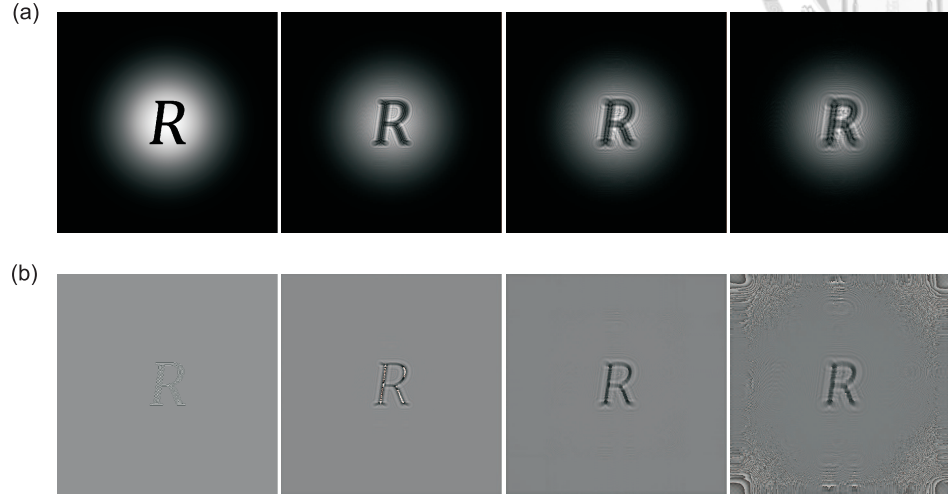
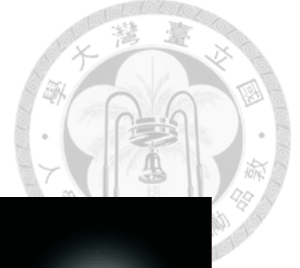


Figure 4.2: (a) Amplitude and (b) phase maps of the numerical diffractions with Fresnel convolution method at $z = 0, 100, 200, 300 \mu m$.

remains constant at various diffraction distances as disclosed in Eq.(4.23). All the fields of view corresponding to the diffraction distances at $z = 0, 100, 200, 300 \mu m$ are $512 \times 512 \mu m^2$.

4.3 Recording of Digital Holograms

A CCD camera serving to record digital holograms consists of a rectangular array of tiny light sensing units, dubbed pixels. One can imagine that nothing subtle will be detected if the interference features of high spatial frequency is smaller than the pixel size. Fairly intuitive, but we want to know how small is small enough.

Consider a simple interference pattern produced by two plane waves on an (x, y) screen. As Figure 4.3 shows, the propagation direction of each plane wave makes a specific angle with the screen normal. For the field amplitudes $E_{1,2}(x) = a_{1,2}(x) \exp[\theta_{1,2}(x)]$, their phase maps on the screen take the forms of $\theta_{1,2}(x, y) = (2\pi/\lambda_{1,2})x \sin \theta_{1,2}$. Recall that Eq.(3.3) provided a mathematical form revealing the behavior of the intensity pattern of the interference.

4.3. RECORDING OF DIGITAL HOLOGRAMS

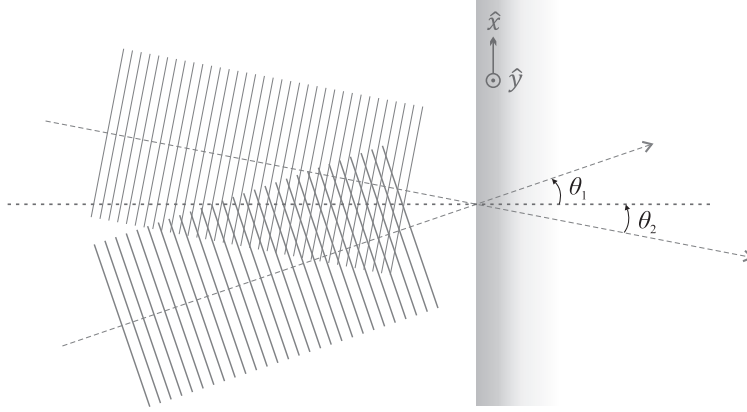


Figure 4.3: Interfering geometry of two plane waves.

Putting the phase maps into the expression that Eq.(3.3) suggests yields

$$I(x, y) = a_1^2(x) + a_2^2(x) + 2 a_1(x) a_2(x) \cos \left[\frac{2\pi}{\lambda_1} x \sin \theta_1 - \frac{2\pi}{\lambda_2} x \sin \theta_2 \right], \quad (4.24)$$

which reaches peak values at multiples of the distance

$$d = \left(\frac{\sin \theta_1}{\lambda_1} - \frac{\sin \theta_2}{\lambda_2} \right)^{-1}. \quad (4.25)$$

In the scenario that $\lambda_1 = \lambda_2 = \lambda$, which is quite common in holographic recording and is exactly the case we study in this thesis,

$$d = \frac{\lambda}{\sin \theta_1 - \sin \theta_2} = \frac{\lambda}{2 \sin \left(\frac{\theta_1 - \theta_2}{2} \right) \cos \left(\frac{\theta_1 + \theta_2}{2} \right)}. \quad (4.26)$$

The maximum spatial frequency to be resolved corresponds to the finest feature with the smallest d at $\theta_2 = -\theta_1 = -\theta$, resulting in

$$f_{max} = \frac{2 \sin \theta_{max}}{\lambda}. \quad (4.27)$$

The Nyquist-Shannon sampling theorem points out that the minimum sampling frequency should be

$$\frac{1}{\Delta x} = 2 f_{max} = \frac{4 \sin \theta_{max}}{\lambda}, \quad (4.28)$$

CHAPTER 4. DIGITAL HOLOGRAPHY

where Δx is the pixel size along the x axis. As a result, the maximum angle subtended by the object and reference waves is limited to

$$\Theta = 2\theta_{max} = 2 \sin^{-1} \frac{\lambda}{4\Delta x}. \quad (4.29)$$

If this were not the case, nothing discernible beyond the Θ can be perceivably detected.





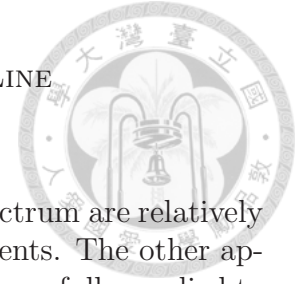
Chapter 5

Twin Image Removal in Digital In-Line Holographic Microscopy

We develop a simple and efficient phase retrieval method based on the iterative inter-projections of the recorded Fourier modulus between two effective holographic planes to eliminate the twin image in digital in-line holography. The proposed algorithm converges stably in phase extraction procedures without requiring any prior knowledge or sophisticated support of the object and is applicable to lensless Gabor and Fourier holography as well as holographic microscopy with imaging lenses. Numerical and experimental results suggest that the spatial resolution enhancement on the reconstructed image can be achieved with this technique due to the capability of recovering the diffraction phases of low-intensity signals.

5.1 Overview of Twin Removal Techniques

Numerous experimental techniques have been developed to overcome the inherent twin image problem since the invention of holography. The spatial separation of the twin image was first demonstrated in off-axis holography by Leith and Upatnieks in 1963 [64]. Using an obliquely incident reference beam can expel the defocused conjugate image from the viewing zone but increases the requirement on the resolution of the recording media. In in-line geometry, single-sideband holography filtering out half of the spatial frequency spectrum in the Fourier plane during the recording and reconstructing processes was shown to be able to spatially isolate the twin image [65]. Similar ideas were explored [66] and extended to double-sideband holography [67].



The experimental setups for manipulating the Fourier spectrum are relatively complicated and may require some extra optical components. The other approach based on the phase-shifting technique has been successfully applied to in-line holography for removing the twin image [68]. Although the complex object can be reconstructed by capturing several interference patterns with different phase shifts, this technique is more suitable for carrying out static imaging.

In addition to those methods, twin image removal has been successfully accomplished with phase retrieval algorithms including hybrid input-output (HIO) [69], difference map [70], oversampling smoothness [71] and guided HIO [72]. The recovery of the lost phases in the recorded hologram is achieved by imposing some constraints or supports on the object and diffraction plane in every iteration of the algorithm. The original object can thus be exactly reconstructed from the full diffraction wave formed by the recorded modulus and the retrieved phases. The reconstruction of the wavefront of the incident wave is also demonstrated successfully without the need of any information on the pupil plane by recording multiple speckle intensity images at various propagation distances [73]. Although the improvement on the data acquisition rate of the speckle intensity measurement is also discussed and optimized [74], the physical movement of the detector and the signal-to-noise ratio may still set the limit on dynamic phase sensing.

In this chapter, we propose a simple and efficient phase retrieval algorithm for removing the twin image in digital in-line holography without setting any constraint in the object plane or requiring prior knowledge about the object. The full phase information of the diffraction wave is obtained by iteratively projecting the recorded hologram between two equivalent holographic planes. The image quality and spatial resolution of the object reconstructed with this novel method is shown to be improved significantly due to the elimination of the conjugate image and the capability of recovering the lost phase of the extremely low-intensity signals in holograms.

5.2 Iterative Phase Retrieval

Optical phases, as noted earlier, cannot be directly measured with electronic devices. But luckily optical waves do carry some innate properties that make their phases manageable with algorithmic manipulations, that is, Fourier transforming the near-field distribution of the wave field to be determined corresponds to their far-field appearance. With this mathematical structure, algorithmic phase retrieval contributes a way for recovering the phase given the measurement of the optical far-field pattern and some other prior



knowledge. In other words, there essentially exists a phase distribution that, when combined with the known Fourier modulus data, satisfy all the prior constraints [70].

The most dominant class of phase-retrieval methods is practicing an iteration scheme that modifies the object in each cycle until the progressively improved Fourier moduli are good enough and all the prior constraints are satisfied. Before an acceptable retrieval is reached, many alternate projections onto different constrained spaces should be performed to facilitate convergence.

5.2.1 Elementary Projectors

The phase problem can be generalized to a problem defined as [75]

Problem. Given two constraint sets \mathcal{S}_1 and \mathcal{S}_2 , find x such that $x \in \mathcal{S}_1 \cap \mathcal{S}_2$.

In almost all practical applications of the physical world we really live in, both \mathcal{S}_1 and \mathcal{S}_2 can be assumed to be subsets of a finite-dimensional Hilbert space \mathbb{H} . The structure of the constraint sets decides whether the problem subject to these sets difficult to solve or not. For example, searching for the solution belonging to $\mathcal{S}_1 \cap \mathcal{S}_2$ will not be thought a challenge provided that both \mathcal{S}_1 and \mathcal{S}_2 are linear constraint spaces. Next, let us move on to the definition of the basic operation – the projection onto a set.

Definition. Let $\mathcal{S} \in \mathbb{H}$ be a closed constraint set. A projection $\mathcal{P}_{\mathcal{S}}$ from an $x \in \mathbb{H}$ onto \mathcal{S} is a mapping that finds a point $\mathcal{P}_{\mathcal{S}}(x) \in \mathbb{H}$ such that $\|x - \mathcal{P}_{\mathcal{S}}(x)\|$ is minimized.

Looking for an answer point in $\mathcal{S}_1 \cap \mathcal{S}_2$ is undoubtedly equivalent to finding out the convergence point of the sequentially alternate projections onto \mathcal{S}_1 and \mathcal{S}_2 from a given initial guess point. Since $x \in \mathcal{S}$ if and only if $x = \mathcal{P}_{\mathcal{S}}(x)$, all solutions to **Problem** satisfy the condition

$$x_{\text{sol}} = \mathcal{P}_{\mathcal{S}_1}(x_{\text{sol}}) = \mathcal{P}_{\mathcal{S}_2}(x_{\text{sol}}). \quad (5.1)$$

Based on this notion, iterative phase-retrieval algorithms are all to reach a final convergence point on $\mathcal{S}_1 \cap \mathcal{S}_2$ through successive alternate projections.

There are many operators that perform fundamental projections, referred to as elementary projectors [76]. Here, we just name a few for helping comprehend their basic operational principles in the language of vector space projection. The first example is the nonnegativity mapping.



Projector 1 (Nonnegativity).

If $\rho(n)$ is the value of pixel n in the object domain, then

$$\rho'(n) = \begin{cases} \rho(n), & \text{if } \rho(n) \geq 0, \\ 0, & \text{otherwise.} \end{cases}$$

For real-valued objects one can impose nonnegativity constraint, setting all negative pixels values to zero and leaving the positive pixel values unchanged. Objects of this kind never assume negative values. For instance, the intensity of a light wave, the instantaneous magnitude of a voltage or current signal, and the probability function of a quantum system, etc. are always nonnegative.

Projector 2 (Support).

Let \mathcal{B} be the support. Support projection is then the mapping

$$\rho'(n) = \begin{cases} \rho(n), & \text{if } n \in \mathcal{B}, \\ 0, & \text{otherwise.} \end{cases}$$

The assumption that the non-support values are 0 is not accurate all the way. In some applications [75], the exit wave emerging from a small isolated specimen immersed in a largely-extended incoming wave is certainly not zero outside the support. This situation should be noted before employing support mapping.

Projector 3 (Modulus).

Let I be the measured intensity profile. Simple modulus projection is the mapping

$$\rho'(n) = \mathcal{F}^{-1} \sqrt{I} \frac{\mathcal{F}\rho(n)}{|\mathcal{F}\rho(n)|}.$$

The modulus projector is a composite operator consisting of two Fourier transformations and one modulus replacement. During alternate Fourier projections, the newly derived phase information is preserved and fed into the next iteration. In our proposed phase-retrieval algorithm that will show up in the later content, only this projector is employed to retrieve the accurate phase footprint of the hologram.

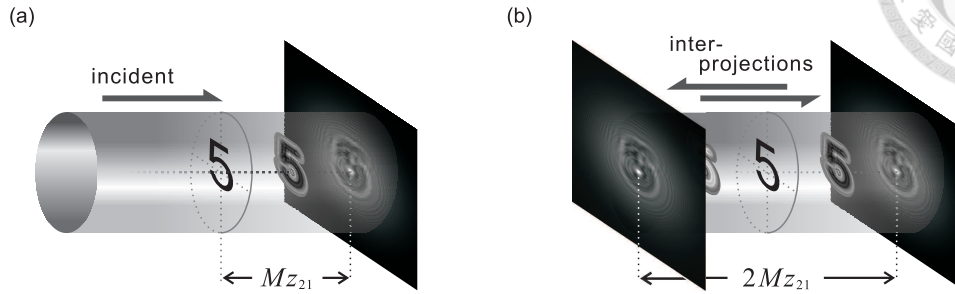


Figure 5.1: (a) Image reconstructed from a diffraction pattern with correct phases. (b) Inter-projections between two identical holograms obtained from Figure 3.5 (a) or Figure 3.5 (b).

5.2.2 Single-Hologram Inter-Projections Algorithm

The twin image problem in holography can be ascribed to the loss of the diffraction phase during recording a hologram. The intensity-only measurement provides two solutions in the conventional image reconstruction method. When the object is numerically reconstructed in digital Fourier holography, the obscured image in the focusing plane arises from the interference of the object field and the diffraction wave of the twin object in inversely symmetric form. In Gabor holography illustrated in Figure 3.5 (b), the reconstructed object is superimposed by the defocused image of an identical twin located on the opposite side of the hologram and at twice the reconstruction distance away from the original object. By providing the correct phase information to the measured hologram, only the original object is restored as it is the inverse process of object diffractions (Figure 5.1 (a)). The object can also be reconstructed from the hologram on the other side by taking the complex conjugate of the diffraction field. As shown in Figure 5.1 (b), the diffraction images on two opposite holographic planes have the same intensity pattern if the test object only modulates the amplitude of the incident wave field [77]. The measured intensity image can thus serve as the constraint in both holographic planes and can be applied to retrieve the diffraction phase.

To obtain the lost diffraction phase information in holograms, we iteratively propagate the wavefield back and forth between the two holographic planes separated by twice the reconstruction distance and apply the field amplitude of the measured hologram as the only constraint. Details of our phase retrieval algorithm between iterations are summarized in the following steps. The first complex diffraction wavefield consists of the field amplitude from the recorded hologram and a randomly assigned phase distribution. The syn-



thesized wavefield numerically propagates to the opposite diffraction plane. Since the intensity pattern on the both planes has to be identical, we replace the modulus of the resulting wavefield with the recorded field amplitude and keep the obtained phase to form the new complex diffraction pattern. The new wavefield then backpropagates to the original diffraction plane. The modulus of the computed wavefield is modified again by the amplitude constraint. The inter-projection of the measured Fourier modulus between the two planes is performed by computing the Rayleigh-Sommerfeld diffraction integral with a simple double fast Fourier transform method, whose formalism takes the form of Eq.(4.22) as an implementation of the Fresnel convolution method in 4.2.2. The iterative procedure repeats until the error between the recorded hologram and the computed squared modulus is smaller than a designated threshold. Once the lost diffraction phase is recovered, the exact object can be reconstructed from the complex diffraction pattern through the inverse process of Eq.(3.18) or Eq.(3.19). It is worth noting that only one elementary projector, modulus mapping in **Projector 3**, involves in the entire phase retrieving process, nothing more.

5.3 Numerical Reconstructions

To verify the reliability and validity of the retrieved phases, we apply the iterative procedure to the image reconstruction for the simulated and experimental holograms. Several numerical simulations and test experiments are demonstrated in the optical regime, paving the way for the holographic reconstruction in Extreme-Ultraviolet Digital Holographic Microscopy.

5.3.1 Proof-of-Concept Simulations

The simulation is performed by assuming that an absorptive figure ‘5’ is illuminated by a focused Gaussian beam following the geometric arrangement in Figure 3.5 (a). The computed Fourier hologram shown in Figure 5.2 (a) is also in the same form as that in Figure 5.2 (b) produced by irradiating a magnified figure ‘5’ with a planar Gaussian beam as verified in Eq.(3.19). By setting the focusing distance as Mz_{21} , the image of the object obtained by using the conventional image reconstruction method is shown in Figure 5.2 (c). The focused object is apparently overlapped with the out-of-focus twin image. A sequence of images reconstructed with our single-hologram inter-projections

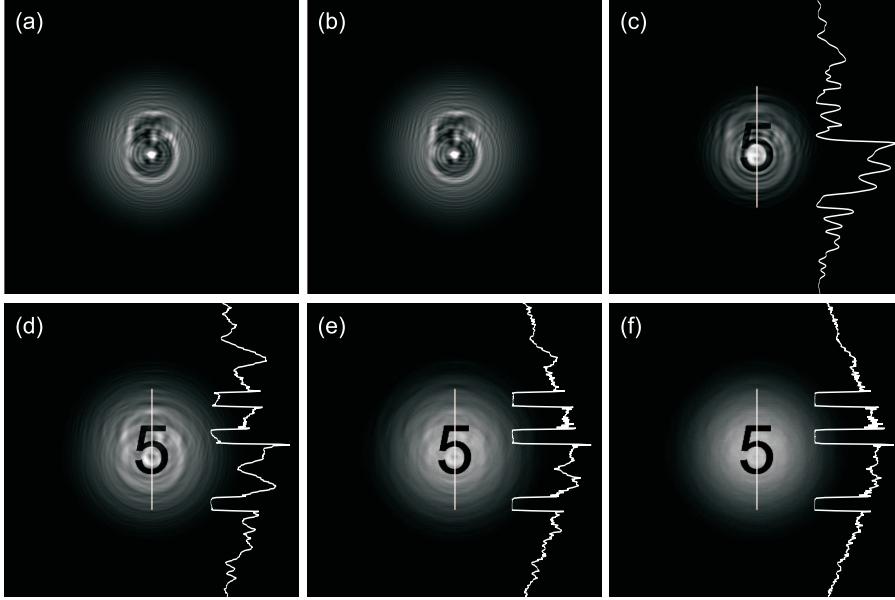
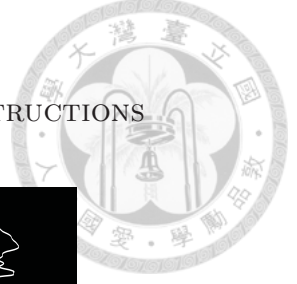


Figure 5.2: Simulated hologram in (a) Fourier's; and (b) Gabor's configuration. (c) Image reconstructed by using the conventional method and (d)-(f) with SHIP method after 1, 10 and 100 iterations respectively. The white curves represent the line profiles along the white line segments.

(SHIP) algorithm is displayed for number of iterations 1, 10 and 100 in Figure 5.2 (d)-(f) respectively.

The curve on the right-hand side of each figure illustrates the intensity profile along the white line segment. After the first iteration, the line scan in Figure 5.2 (d) indicates the image with higher intensity contrast and sharper edge response is obtained by using SHIP method. As iterations increase, the suppression of the twin image becomes evident and the disturbance-free object is reconstructed. The convergence of the iterative algorithm is also monitored by calculating the normalized squared error defined as

$$\delta_i = \frac{\sum_{n=1}^N \left[|G_i(n)| - |U_2(n)| \right]^2}{\sum_{n=1}^N |U_2(n)|^2}, \quad (5.2)$$

where $G_i(n)$ represents the new diffraction field in the n_{th} pixel after the i_{th} reconstruction at $z = z_2$ and $U_2(n)$ is the measured field distribution. The errors of the diffraction intensity in Figure 5.2 are estimated to be (d) 2×10^{-2} , (e) 1×10^{-4} and (f) 9×10^{-6} . For a hologram of $1,023 \times 1,023$ pixels, the reconstruction process for achieving an error $\delta < 10^{-4}$ requires 11 iterations, taking only a few seconds on a personal computer. The original simulated

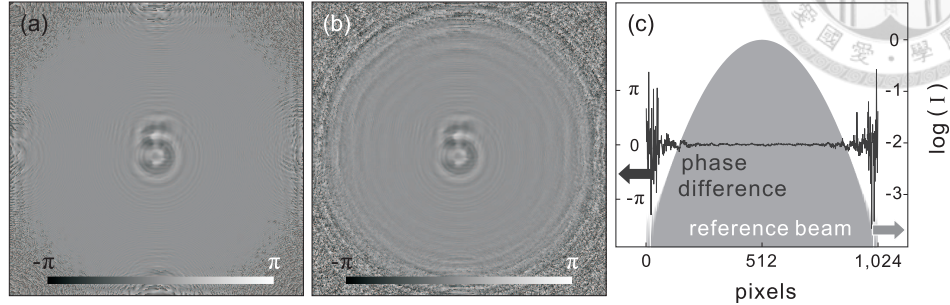


Figure 5.3: (a) Simulated and (b) reconstructed phase pattern of Figure 5.2 (b); (c) The error of the reconstructed phase pattern (solid line) and the normalized intensity profile of the reference beam on the detection plane.

and the retrieved phase pattern of the diffraction wave of Figure 5.2 (b) are shown in Figures 5.3 (a) and 5.3 (b) respectively. The discrepancy between the diffraction phases obtained with the SHIP algorithm after 100 iterations and the theoretical values in the simulation is shown in Figure 5.3 (c). The shaded area denotes the intensity profile along the center of the incident reference beam on the detection plane. Negligible errors in the retrieved phases are found to cover the region of the diffraction pattern down to the normalized reference intensity level of 10^{-3} , much wider than the $1/e^2$ width of the Gaussian reference beam. The accessible high-spatial-frequency signals in the diffraction pattern improve the imaging resolution of the conventional digital holography by a factor of ~ 1.8 . In addition, the proposed phase retrieval method also enables us to perform high-resolution imaging without requiring a distinct boundary in the field of the object plane.

Robustness of reconstructing holograms over a wide range of signal-to-noise ratios is verified and shown in Figure 5.4. In this demonstration, we artificially introduce Gaussian white noise with different noise level into the simulated hologram, Figure 5.2 (b), to provide SHIP algorithm with a series of noisy holograms for subsequent reconstructions. As clear it reveals from the reconstructions in Figure 5.4, the capability of twin image removal in noise-free case is also guaranteed by the SHIP method to noisy holograms. Even to that suffering from severe noise contamination, $\text{SNR} = 0$ dB in Figure 5.4 (d), removing its twin image via SHIP method still works only at the expense of image contrast.

A 3D absorptive object consisting of a figure ‘5’ and a rectangular mesh at different locations in the z -axis is also used to test the proposed algorithm, whose holographic recording geometry is illustrated in Figure 5.5 (a). The numerical reconstructions of the 3D object are carried out by using the con-

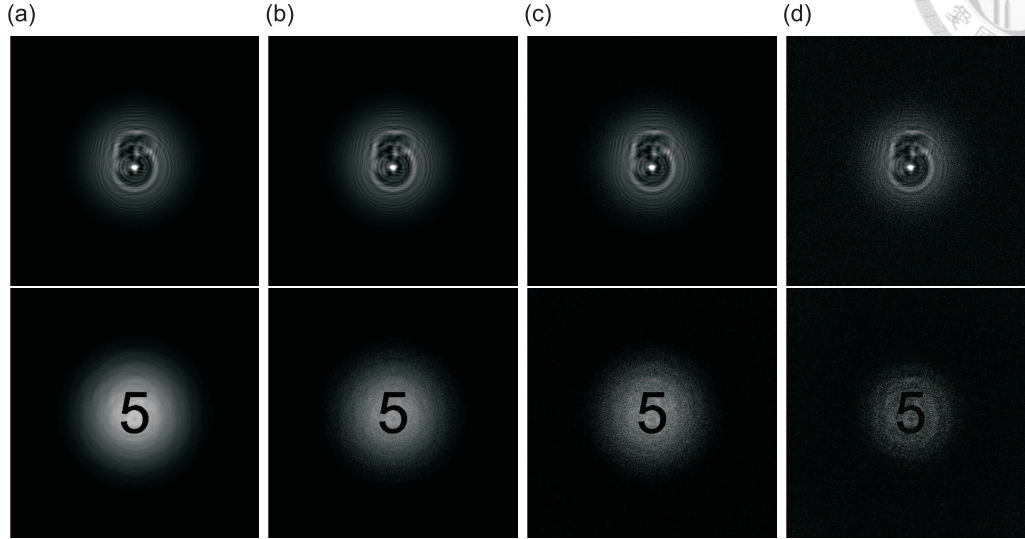


Figure 5.4: Simulated holograms under different signal-to-noise ratios (SNR) in the upper row and their corresponding reconstructions from 100 iterations of SHIP algorithm in the lower row. (a) Noise-free. (b) SNR = 40 dB. (c) SNR = 20 dB. (d) SNR = 0 dB.

ventional technique and SHIP method, and the results are shown in Figures 5.5 (b) and (c) accordingly. It is apparent that only one corresponding part of the object is best focused at each plane while the other part of the object remains out of focus. Furthermore, the result shown in Figure 5.5 (c) is also free from the disturbing twin image. This result indicates that the 3D object is successfully reconstructed with the SHIP algorithm. It should be noted that the introduction of the feedback parameter β defined in the HIO algorithm [69] on the new estimated field in our phase retrieval method does not improve the efficiency or accuracy in the image reconstruction shown above. A uniform phase pattern instead of a random one assigned at the beginning of the algorithm generally results in faster convergence in phase retrieval.

5.3.2 Proof-of-Concept Experiments

To further assess the validity of the algorithm, we have tested the proposed method on the experimental data obtained from in-line Fourier holography as illustrated in Figure 3.5 (a). A positive lens of a focal length of 80 mm was used to focus a 632.8-nm He-Ne laser beam in a Gaussian profile to form

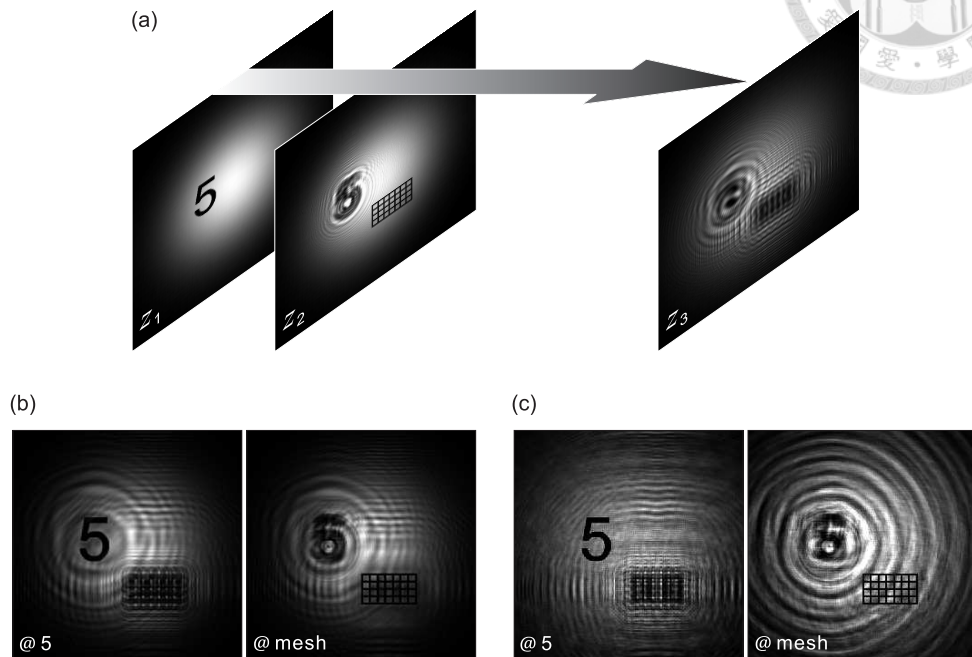


Figure 5.5: (a) Holographic recording geometry. (b) Reconstructions of the object at different depths with the conventional method and (c) SHIP method.

a point-like light source for imaging. A numeric ‘5’ deposited on a positive USAF 1951 resolution target was placed into the divergent laser beam and served as the test object. The corresponding holograms were recorded by a 14-bit CCD camera with a 768×512 array of $9\text{-}\mu\text{m}$ square pixels. By translating the test object toward or away from the focal spot, an adjustable field of view and magnification of holographic imaging can be achieved. Figure 5.6, from left to right respectively, shows the recorded holograms and the corresponding images of the test object reconstructed by using the conventional method and SHIP technique with three different magnifications: (a) $M = 5$, (b) $M = 7.5$ and (c) $M = 9.5$. The twin images obviously fade away after applying 100 iterations in SHIP method. As the numerical aperture of the focused Gaussian beam is around 0.032, the theoretical spatial resolution of digital Fourier holography is estimated to be $\sim 9.8\ \mu\text{m}$. The best spatial resolution of the conventional holographic image in Figure 5.6 (c) is measured to be $\sim 10.9\ \mu\text{m}$ while the 10/90 edge response of the image reconstructed with the SHIP algorithm is nearly $5.7\ \mu\text{m}$, almost half that from the conventional method. The demonstration of high-resolution holographic imaging can therefore be attributed to the elimination of the twin image and the con-

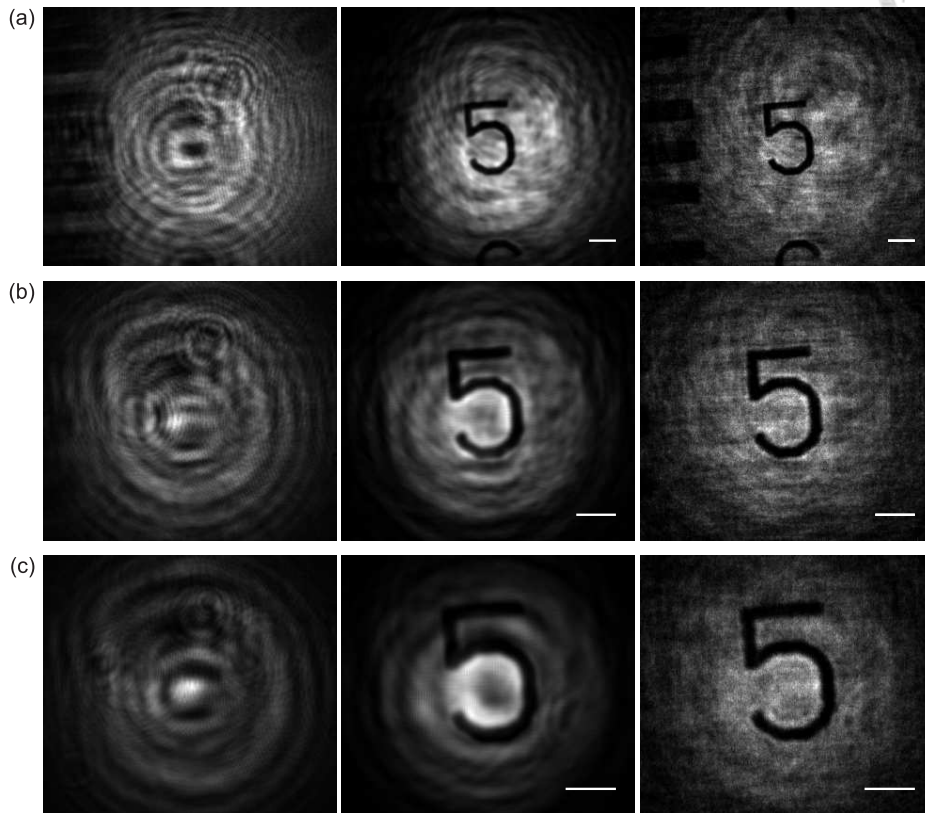
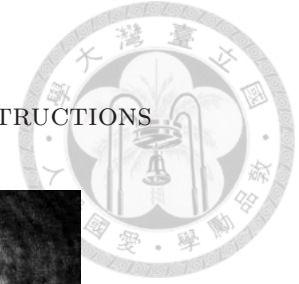


Figure 5.6: Experimental measurements and reconstructed images with imaging magnifications of (a) $M = 5$, (b) $M = 7.5$ and (c) $M = 9.5$. From left to right : recorded holograms, reconstructions with the conventional method and reconstructions with SHIP method. The scale bars in the figures represent $50 \mu\text{m}$ in length.

tribution of high-spatial-frequency signals with the correct diffraction phases.

5.3.3 Extreme-Ultraviolet Digital Holographic Microscopy

We finally turn our attention to EUV Digital Holographic Microscopy (DHM), which uses Ni-like Krypton laser at 32.8 nm for holographic recording within an experiment layout depicted in Figure 5.7 (a).

The generation mechanism of the light source has been elucidated in Chapter 1 and Chapter 2. Some characteristic parameters of the EUV laser

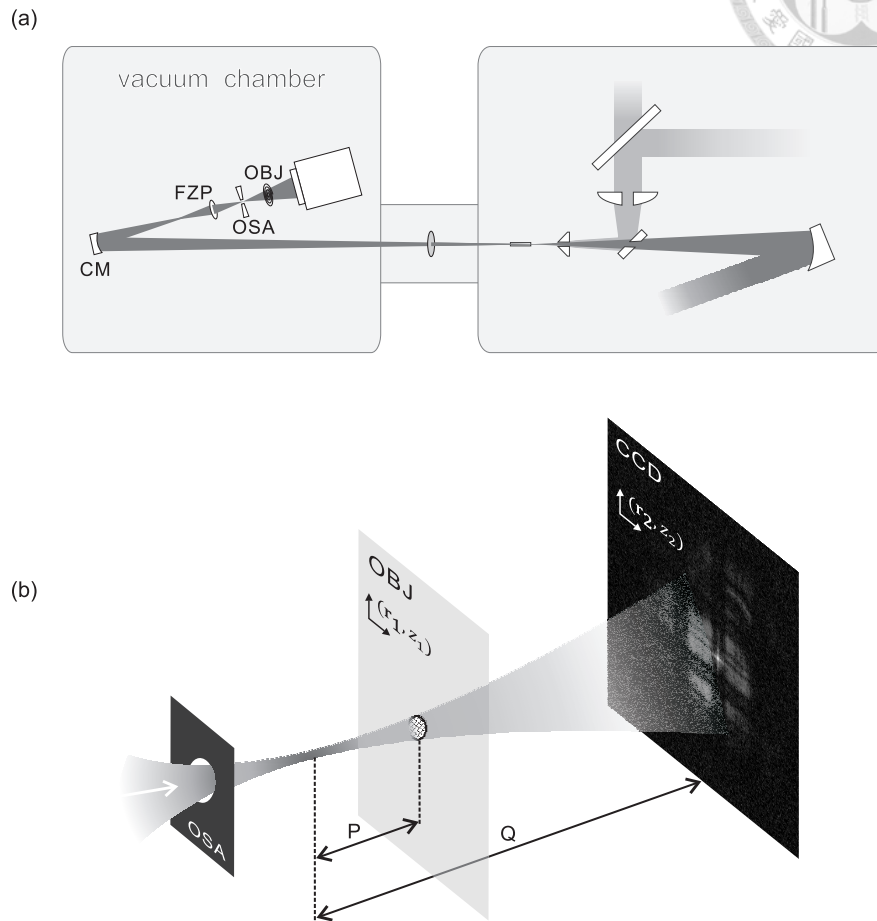


Figure 5.7: (a) Experiment layout. CM: EUV concave mirror, FZP: Fresnel zone plate, OSA: order-sorting aperture, OBJ: object. (b) P: distance of object from the focus of the EUV laser beam, Q: distance of CCD camera from the focus of the EUV laser beam.

adopted in this subsection are that its output reached 8×10^{10} photons per shot with a beam divergence as small as 5.6 mrad in full width at half maximum (FWHM), and that the spatial coherence length was measured to be 95 μm a distance of 25 cm from the laser [45]. The EUV holographic microscope consists of a Mo/B₄C/Si multilayer concave mirror with a reflectivity of 19% at 32.8 nm, an imaging Fresnel zone plate, an order-sorting aperture and a 16-bit back-illuminated x-ray CCD camera with a 1024×1024 array of 13- μm pixels. A 0.25- μm -thick aluminum filter was inserted at the output of the EUV laser to block the copropagating pump pulse, preventing the remaining unabsorbed pump wave from impinging on the x-ray CCD. An EUV concave mirror of 30-cm focal length served as a condenser for the imaging optics

5.3. NUMERICAL RECONSTRUCTIONS



downstream, and simultaneously played an important role of sieving out the desired 32.8-nm photons. A freestanding 100-nm -thick Si_3N_4 Fresnel zone plate for imaging is fabricated with electron beam lithography by NanoX Laboratory of Institute of Physics in Academia Sinica, which has a diameter of $550\ \mu\text{m}$ and comprises 1,350 zones of progressively narrowing zonal width down to $102\ \text{nm}$ outermost. Plenty of 80-nm -wide struts are fabricated as well during the manufacturing process for mechanically connecting each zone and supporting the whole piece. The physical structure of the Fresnel zone plate is inspected with a Scanning Electron Microscope (SEM), whose SEM images under different magnifications are shown in Figure 5.8. With respect to 32.8-nm coherent EUV source, the Fresnel zone plate has a numerical aperture $\text{NA}=0.16$, corresponding to a focal length of $1.7\ \text{mm}$. The distance between the imaging zone plate and CCD camera was approximately $52\ \text{mm}$. One of the two objects selected as the test samples is a Fresnel zone plate that is identical to the imaging zone plate but with a local fractured structure, and the other one is a two-dimensional 20-nm -thick carbon-foil square mesh array of $7\ \mu\text{m} \times 7\ \mu\text{m}$ holes with $2\text{-}\mu\text{m}$ bars in between. The objects were mounted on a motorized translation stage capable of moving parallel to the direction of EUV laser beam propagation.

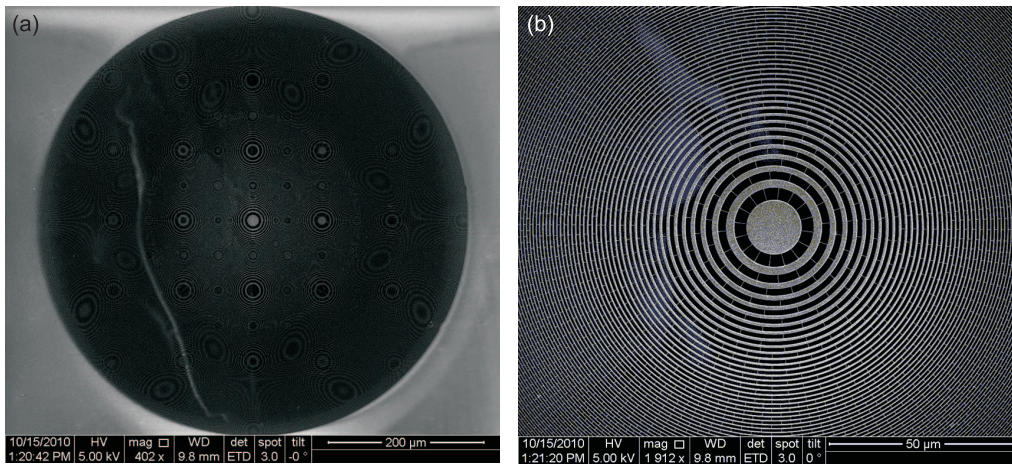


Figure 5.8: Nanostructures of the imaging Fresnel zone plate observed with a Scanning Electron Microscope under magnifications of (a) $M = 402$ and (b) $M = 1912$. (Courtesy of NanoX Lab., Academia Sinica, Taiwan)

High-contrast holographic images with single picosecond EUV exposures were obtained through focusing the EUV laser beam on the test object and subsequently gathering the strong scattering signal. The action of focusing was implemented with a Fresnel zone plate followed by an order-sorting aper-

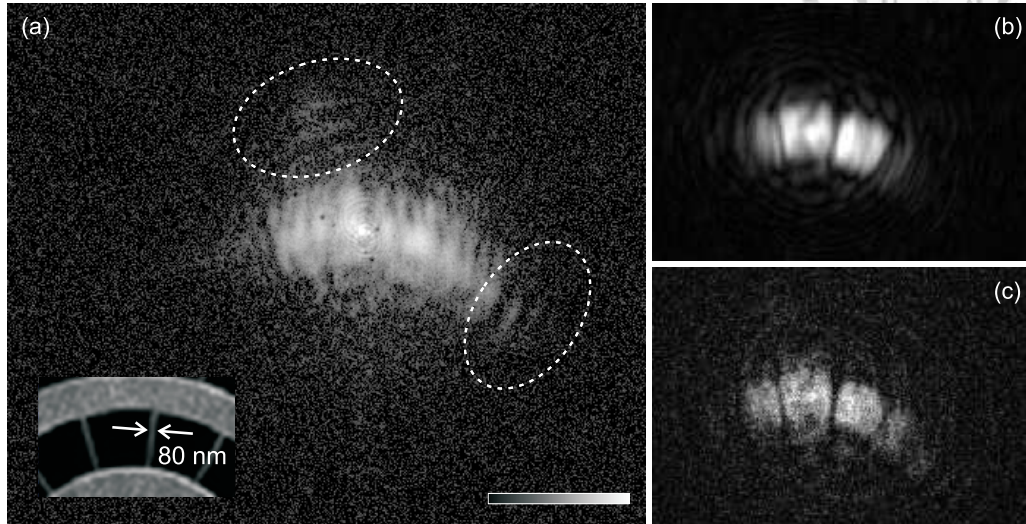


Figure 5.9: (a) Digital EUV hologram of the zone plate zonal structure with a magnification of 174, and the inset is the SEM object image of the corresponding region. Patterns located by dashed ellipses are diffraction signals with weak reference illumination. (b) Reconstruction from the conventional DHM algorithm. (c) Reconstruction from the SHIP algorithm.

ture for blocking the zeroth and other higher-order radiations, which is shown in Figure 5.7 (a). The tight focusing point was viewed as the point source for the configuration of Fourier holography illustrated in Figure 3.5 (a). Both the object and reference waves were diverging spherical waves with almost the same curvature perceived by the CCD camera. As illustrated in Figure 5.7 (b), the imaging zone plate produces a magnified diffraction pattern on the CCD camera with a geometric magnification $M = Q/P$. Moving the test object toward the focusing point of the incoming EUV beam leads to an even larger magnified image at the cost of a smaller field of view. Several holograms corresponding to different magnifications were thus prepared for subsequent numerical reconstructions. In the following discussion, we apply both the conventional reconstruction method and SHIP algorithm to all these holograms for qualitative and quantitative comparisons of their respective algorithmic performances.

Figure 5.9 (a) shows the single-shot EUV hologram of the zone plate's inner zonal structure recorded by an x-ray CCD camera with a magnification of 174. The mechanism for EUV lasing by virtue of the optically-preformed plasma waveguide technique entails formation of speckles whose sizes depend on the source size [5], leading to the spatial nonuniformity in the hologram other than the granular background thermal noise. The inset in Figure 5.9 (a)

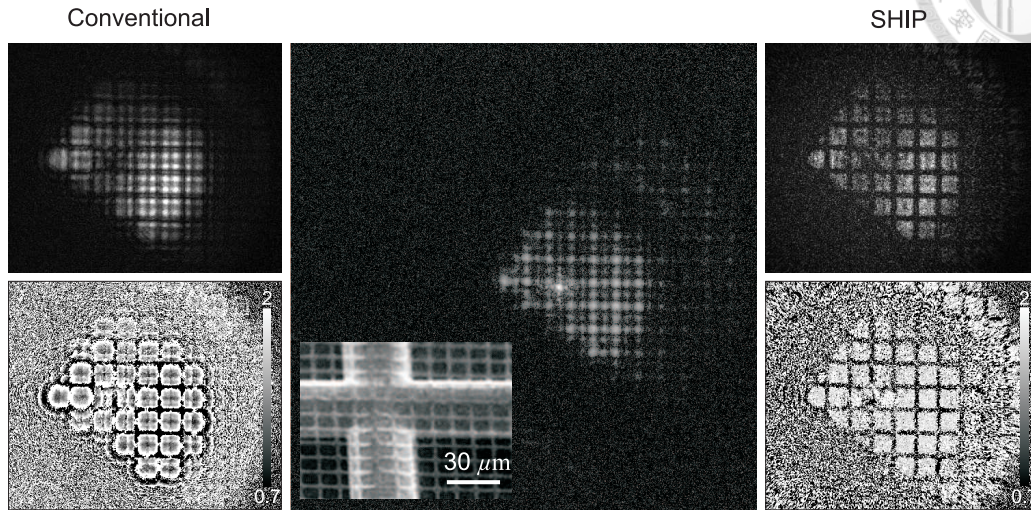


Figure 5.10: Magnification $M = 73$. Comparison of the reconstruction results from the conventional and SHIP methods. The inset at the corner of the hologram pattern is the SEM image of a carbon-foil mesh.

is the SEM image of the original object, showing some interzonal struts with 80-nm width. With a proper choice of the reconstruction distance, two intensity images of the local zonal structure of the zone plate sample are derived and shown in Figure 5.9 (b)(c), which correspond to the reconstructions from the conventional DHM algorithm and SHIP algorithm respectively. It is evident from Figure 5.9 (b) that the existence of the twin image seriously mars the reconstruction quality, while the reconstruction in Figure 5.9 (c) is nearly free from the twin disturbance.

Another test sample, a carbon-foil mesh, was studied as well under the same experimental setup. A series of EUV holograms with different magnifications were recorded, two of them are picked out here for demonstrating and letting us appreciate the superiority of the SHIP algorithm over the conventional method. Figure 5.10 shows the case under magnification $M = 73$, the center of which is the hologram with an inset of the object's SEM image at the corner. The left column from top to bottom are the reconstructed intensity and phase patterns derived from the conventional method, while the right column are their counterparts from the SHIP method. As to image fidelity, the intensity pattern from the SHIP method apparently outranks the result from its rival. Besides, the phase retrieved from the SHIP algorithm appears uniform and smoother within each mesh, as it should be in the real object. Other than the phase uniformity, something really exciting catches our eye. Comparing those two phase maps, we find the upper right

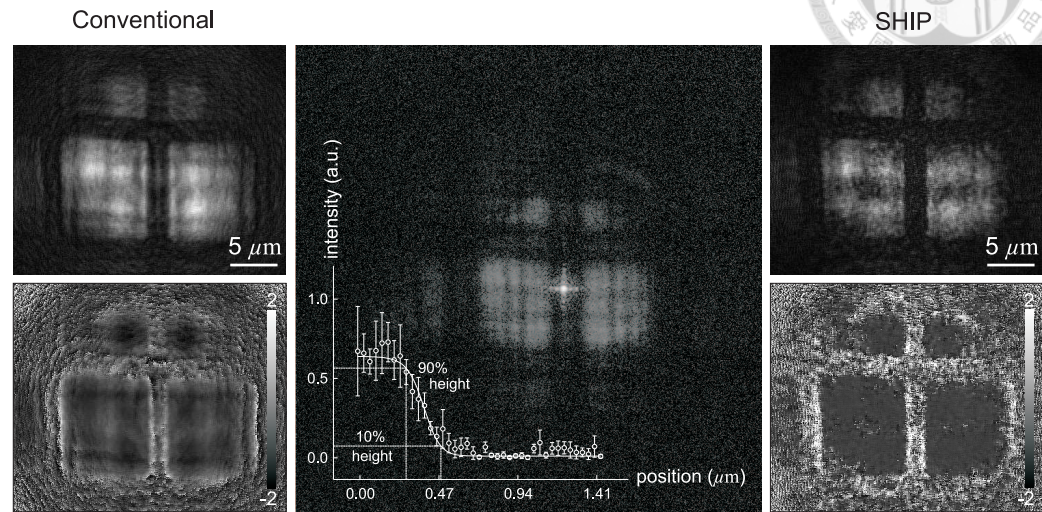


Figure 5.11: Magnification $M = 363$. Comparison of the reconstruction results from the conventional and SHIP methods. The inset at the corner of the hologram pattern is the 10/90 edge response of the SHIP intensity reconstruction.

region to be retrieved successful in the SHIP case, but totally failed by the conventional method, which confirms the prediction suggested by the aforementioned Proof-of-Concept Simulations and Experiments that the SHIP algorithm is capable of recovering the diffraction phases of low-intensity signals. Both the reconstructed phase maps share the same grey-scale bar as attached in the figures.

We then pushed our imaging system to its limit, a magnification of $M = 363$ was pursued. Figure 5.11 shows the case under magnification $M = 363$ and likewise, the reconstructions from the two method are separately put on the two sides of the central hologram. Under such magnification, characterization of image fidelity is examined quantitatively. The inset at the corner of the hologram reveals the 10/90 edge response of the reconstructed intensity image from the SHIP method, where the edge response is derived from the logistic fitting of the five sets of transverse intensity measurements along a sharp edge. The best spatial resolution of this SHIP reconstruction is measured to be around 215 nm , while that of the reconstruction from the conventional method is nearly 297 nm . The NA of the system in this measurement was estimated to be 0.13, corresponding to a theoretical spatial resolution of around 150 nm . Incidentally from the phase map retrieved by the SHIP algorithm, the thickness of the carbon film is deduced to be $28\sim 38\text{ nm}$, corresponding to the phase delays of $1.2\sim 1.6\text{ rad}$. According to

5.3. NUMERICAL RECONSTRUCTIONS

the specification of such commercial product, the canonical thickness of the carbon films lies between $20 \sim 30 \text{ nm}$.

Again, as we have already learned from the previous experience, the demonstration of our twin-free digital holographic microscopy does prove its core SHIP algorithm to perform better than the conventional DHM method. Spatial resolvability of our technique can be further improved by adopting imaging systems with even larger numerical aperture, cameras possessing the ability for achieving higher signal-to-noise ratios, and illuminations with shorter-wavelength sources. The superiority of high-resolution holographic imaging based on the SHIP algorithm can be arguably attributed to the elimination of twin image and the contribution of high-spatial-frequency signals with the correct diffraction phases.

CHAPTER 5. TWIN IMAGE REMOVAL IN DIGITAL IN-LINE
HOLOGRAPHIC MICROSCOPY





Chapter 6

Conclusion and Perspective

High-brightness OFI collisional-excitation EUV lasing of Ni-like krypton at 32.8 nm pumped by the 100-TW laser system is demonstrated. An average output of 10^{12} photons per pulse for 32.8-nm laser at a pump energy of less than 1 J is achieved with an optically preformed plasma waveguide fabricated by using the axicon-ignitor-heater scheme, and the corresponding energy conversion efficiency reaches an unprecedentedly high level of around 10^{-5} . The far-field pattern of the laser changes with increasing pump energies from a single peak to an annular profile due to over-ionization of krypton ions at the center of the plasma channel. Running at a 10-Hz repetition rate, the EUV laser is capable of supporting applications that require high repetition rate. Its large photon number per pulse is also an advantage for coherent flash imaging.

With a well-developed and stable EUV coherent source in hand, opportunities for improving the imaging performance of holographic microscopy in this spectral regime are exploited. A novel phase retrieval method for solving the twin image problem in digital Fourier holography is developed and demonstrated numerically and experimentally. The information required in the iterative algorithm is simply one recorded hologram. The proposed method not only can be applied to the coherent imaging with lensless Gabor holography and Fourier holography but also can be adapted for holographic microscopy with imaging lenses. For a hologram recorded in high signal-to-noise ratio, the spatial resolution of the reconstructed image may be enhanced dramatically as the phases of the signals at low intensity and large diffraction angles can be retrieved accurately. Although the spatial resolution demonstrated with the SHIP algorithm cannot be as high as that obtained by coherent diffractive imaging, the most attractive features of this technique are that the image reconstruction process is simple and efficient and can easily be applied to achieve volume holographic imaging especially

CHAPTER 6. CONCLUSION AND PERSPECTIVE



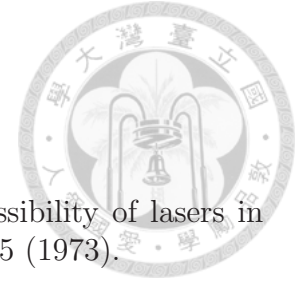
for the twin image located very close to the reconstructed object in x-ray or gamma-ray holography [78, 79].

We are just beginning to get the picture of the SHIP algorithm. Although quite promising it looks so far, yet, a full performance characterization still needs to be examined. In modern biophysical experiments, microscopy is often employed to visualize the microstructure of biological samples. Objects of this kind almost carry complex phase footprints. For that very reason, reconstructions of those highly complex but practical objects via the SHIP method are worth studying much more thoroughly before claiming its universal applicability.



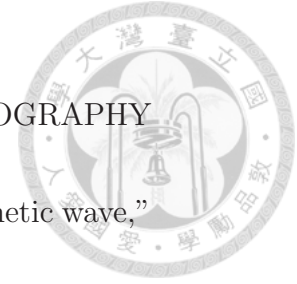
Bibliography

- [1] D. Attwood, *Soft X-Rays and Extreme Ultraviolet Radiation: Principles and Applications* (Cambridge University Press, Cambridge, 2007).
- [2] M. C. Chou, "Experimental study of optical-field-ionization collisional-excitation soft x-ray lasers," Ph.D. Thesis - National Chung Cheng University (2007).
- [3] H. H. Chu, "Construction of a 10-tw laser of high coherence and stability and its application in laser-cluster interaction and x-ray lasers," Ph.D. Thesis - National Taiwan University (2005).
- [4] M.-C. Chou, P.-H. Lin, C.-A. Lin, J.-Y. Lin, J. Wang, and S.-Y. Chen, "Dramatic enhancement of optical-field-ionization collisional-excitation x-ray lasing by an optically preformed plasma waveguide," *Phys. Rev. Lett.* **99**, 063,904 (2007).
- [5] B. K. Chen, Y. C. Ho, T. S. Hung, Y. L. Chang, M. C. Chou, S. Y. Chen, H. H. Chu, S. L. Huang, P. H. Lin, J. Wang, and J. Y. Lin, "High-brightness optical-field-ionization collisional-excitation extreme-ultraviolet lasing pumped by a 100-TW laser system in an optically preformed plasma waveguide," *Appl. Phys. B* **106**, 817–822 (2012).
- [6] R. C. Elton, *X-ray lasers* (Academic Press, San Diego, CA, 1990).
- [7] J. J. Rocca, "Table-top soft x-ray lasers," *Rev. Sci. Instrum.* **70**, 3799–3827 (1999).
- [8] A. E. Siegman, *Lasers* (University Science Books, 55D Gate Five Road, Sausalito, CA 94965, USA, 1986).
- [9] A. G. Molchanov, "Lasers in the vacuum ultraviolet and in the x-ray regions of the spectrum," *Sov. Phys. Usp.* **15**, 124–129 (1972).
- [10] R. C. Elton, "Extension of $3p \rightarrow 3s$ ion lasers into the vacuum ultraviolet region," *Appl. Opt.* **14**, 97–101 (1975).



BIBLIOGRAPHY

- [11] A. V. Vinogradov and I. I. Silverman, "On the possibility of lasers in the uv and x-ray ranges," *Sov. Phys. JETP* **36**, 1115 (1973).
- [12] D. L. Matthews, P. L. Hagelstein, M. D. Rosen, M. J. Eckart, N. M. Ceglio, A. U. Hazi, H. Medecker, B. J. MacGowan, J. E. Trebes, B. L. Whitten, E. M. Campbell, C. W. Hatcher, A. M. Hawryluk, R. L. Kauffman, L. D. Pleasance, G. Rambach, J. H. Scofield, G. Stone, and T. A. Weaver, "Demonstration of a soft x-ray amplifier," *Phys. Rev. Lett.* **54**, 110–113 (1985).
- [13] A. Prag, A. Glinz, J. Balmer, Y. Li, and E. Fill, "Prepulse dependence of J=0-1 lasing at 32.6 nm in neon-like titanium," *Appl. Phys. B* **63**, 113–116 (1996).
- [14] H. Daido, K. Murai, R. Kodama, G. Yuan, M. Schulz, M. Takagi, Y. Kato, D. Neely, A. MacPhee, and C. Lewis, "Collisional excitation soft X-ray laser at 23.6 nm in a laser-produced cylindrical target," *Appl. Phys. B* **62**, 129–133 (1996).
- [15] F. G. Tomasel, J. J. Rocca, V. N. Shlyaptsev, and C. D. Macchietto, "Lasing at 60.8 nm in ne-like sulfur ions in ablated material excited by a capillary discharge," *Phys. Rev. A* **55**, 1437–1440 (1997).
- [16] B. R. Benware, C. D. Macchietto, C. H. Moreno, and J. J. Rocca, "Demonstration of a high average power tabletop soft x-ray laser," *Phys. Rev. Lett.* **81**, 5804–5807 (1998).
- [17] Y. V. Afanas'ev and V. N. Shlyaptsev, "Formation of a population inversion of transitions in Ne-like ions in steady-state and transient plasmas," *Sov. J. Quantum Electron.* **19**, 1606–1612 (1989).
- [18] P. V. Nickles, V. N. Shlyaptsev, M. Kalachnikov, M. Schnürer, I. Will, and W. Sandner, "Short pulse x-ray laser at 32.6 nm based on transient gain in ne-like titanium," *Phys. Rev. Lett.* **78**, 2748–2751 (1997).
- [19] J. Dunn, A. L. Osterheld, R. Shepherd, W. E. White, V. N. Shlyaptsev, and R. E. Stewart, "Demonstration of x-ray amplification in transient gain nickel-like palladium scheme," *Phys. Rev. Lett.* **80**, 2825–2828 (1998).
- [20] N. H. Burnett and P. B. Corkum, "Cold-plasma production for recombination extreme-ultraviolet lasers by optical-field-induced ionization," *J. Opt. Soc. Am. B* **6**, 1195–1199 (1989).



- [21] L. V. Keldysh, "Ionization in the field of a strong electromagnetic wave," *Sov. Phys. JETP* **20**, 1307–1314 (1965).
- [22] B. H. Bransden and C. J. Joachain, *Physics of Atoms and Molecules* (Prentice Hall, 2nd ed., 2002).
- [23] E. Goulielmakis, *Complete Characterization of Light Waves using Attosecond Pulses* (Ph.D. Thesis - Ludwig Maximilians Universität, 2005).
- [24] M. V. Ammosov, N. B. Delone, and V. P. Krainov, "Tunnel ionization of complex atoms and atomic ions in an alternating electromagnetic field," *Sov. Phys. JETP* **64**, 1191–1196 (1986).
- [25] A. Scrinzi, M. Geissler, and T. Brabec, "Ionization above the coulomb barrier," *Phys. Rev. Lett.* **83**, 706–709 (1999).
- [26] P. B. Corkum, N. H. Burnett, and F. Brunel, "Above-threshold ionization in the long wavelength limit," *Phys. Rev. Lett.* **62**, 1259–1262 (1989).
- [27] R. R. Freeman, P. H. Bucksbaum, H. Milchberg, S. Darack, D. Schumacher, and M. E. Geusic, "Above-threshold ionization with subpicosecond laser pulses," *Phys. Rev. Lett.* **59**, 1092–1095 (1987).
- [28] S. Sebban, R. Haroutunian, P. Balcou, G. Grillon, A. Rousse, S. Kazamias, T. Marin, J. P. Rousseau, L. Notebaert, M. Pittman, J. P. Chambaret, A. Antonetti, D. Hulin, D. Ros, A. Klisnick, A. Carillon, P. Jaeglé, G. Jamelot, and J. F. Wyart, "Saturated amplification of a collisionally pumped optical-field-ionization soft x-ray laser at 41.8 nm," *Phys. Rev. Lett.* **86**, 3004–3007 (2001).
- [29] A. Butler, A. J. Gonsalves, C. M. McKenna, D. J. Spence, S. M. Hooker, S. Sebban, T. Mocek, I. Bettaibi, and B. Cros, "Demonstration of a collisionally excited optical-field-ionization xuv laser driven in a plasma waveguide," *Phys. Rev. Lett.* **91**, 205,001 (2003).
- [30] T. Mocek, C. M. McKenna, B. Cros, S. Sebban, D. J. Spence, G. Maynard, I. Bettaibi, V. Vorontsov, A. J. Gonsalves, and S. M. Hooker, "Dramatic enhancement of xuv laser output using a multimode gas-filled capillary waveguide," *Phys. Rev. A* **71**, 013,804 (2005).
- [31] B. Cros, T. Mocek, I. Bettaibi, G. Vieux, M. Farinet, J. Dubau, S. Sebban, and G. Maynard, "Characterization of the collisionally pumped optical-field-ionized soft-x-ray laser at 41.8nm driven in capillary tubes," *Phys. Rev. A* **73**, 033,801 (2006).



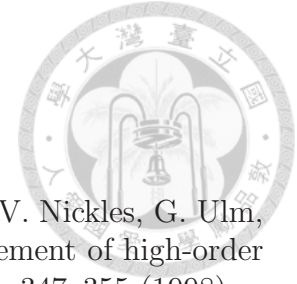
BIBLIOGRAPHY

- [32] P. H. Lin, “Development of multi-line and seeded waveguide-based soft x-ray lasers,” Ph.D. Thesis - National Taiwan University (2010).
- [33] V. V. Korobkin, L. Y. Polonskii, V. P. Poponin, and L. N. Pyatnitskii, “Focusing of Gaussian and super-Gaussian laser beams by axicons to obtain continuous laser sparks,” *Sov. J. Quantum Electron.* **16**, 178–182 (1986).
- [34] A. G. Sedukhin, “Beam-preshaping axicon focusing,” *J. Opt. Soc. Am. A* **15**, 3057–3066 (1998).
- [35] W. L. Kruer, *The physics of laser plasma interactions* (Addison-Wesley Publishing Company, 1988).
- [36] M. Moll, T. Bornath, M. Schlanges, and V. P. Krainov, “Inverse bremsstrahlung heating rate in atomic clusters irradiated by femtosecond laser pulses,” *Phy. Plasma* **19** (2012).
- [37] C. G. Durfee III, J. Lynch, and H. M. Milchberg, “Development of plasma waveguide for high-intensity laser pulses,” *Phys. Rev. E* **51**, 2368–2389 (1995).
- [38] T.-S. Hung, C.-H. Yang, J. Wang, S.-Y. Chen, J.-Y. Lin, and H.-H. Chu, “A 110-TW multiple-beam laser system with a 5-TW wavelength-tunable auxiliary beam for versatile control of laser-plasma interaction,” *Appl. Phys. B* **117**, 1189–1200 (2014).
- [39] T. Kita, T. Harada, N. Nakano, and H. Kuroda, “Mechanically ruled aberration-corrected concave gratings for a flat-field grazing-incidence spectrograph,” *Appl. Opt.* **22**, 512–513 (1983).
- [40] Y.-F. Xiao, H.-H. Chu, H.-E. Tsai, C.-H. Lee, J.-Y. Lin, J. Wang, and S.-Y. Chen, “Efficient generation of extended plasma waveguides with the axicon ignitor-heater scheme,” *Phys. Plasmas* **11**, L21–L24 (2004).
- [41] S. C. Wilks, J. M. Dawson, W. B. Mori, T. Katsouleas, and M. E. Jones, “Photon Accelerator,” *Phys. Rev. Lett.* **62**, 2600–2603 (1989).
- [42] C. H. Moreno, M. C. Marconi, V. N. Shlyaptsev, B. R. Benware, C. D. Macchietto, J. L. A. Chilla, J. J. Rocca, and A. L. Osterheld, “Two-dimensional near-field and far-field imaging of a ne-like ar capillary discharge table-top soft-x-ray laser,” *Phys. Rev. A* **58**, 1509–1514 (1998).



BIBLIOGRAPHY


- [43] P.-H. Lin, M.-C. Chou, M.-J. Jiang, P.-C. Tseng, H.-H. Chu, J.-Y. Lin, J. Wang, and S.-Y. Chen, “Seeding of a soft-x-ray laser in a plasma waveguide by high harmonic generation,” *Opt. Lett.* **34**, 3562–3564 (2009).
- [44] H. Ghasem, G. H. Luo, and A. Mohammadzadeh, “Utilization of transverse deflecting RF cavities in the designed QBA lattice of 3 GeV Taiwan Photon Source,” *J. Instrum.* **5** (2010).
- [45] P.-H. Lin, M.-C. Chou, C.-A. Lin, H.-H. Chu, J.-Y. Lin, J. Wang, and S.-Y. Chen, “Optical-field-ionization collisional-excitation x-ray lasers with an optically preformed plasma waveguide,” *Phys. Rev. A* **76**, 053,817 (2007).
- [46] http://www.aps.anl.gov/epics/meetings/2011-06/sys/data/85/TLS_TPS-status_2011_0214_1.pdf.
- [47] A. Rundquist, C. Durfee, Z. Chang, C. Herne, S. Backus, M. Murnane, and H. Kapteyn, “Phase-matched generation of coherent soft X-rays,” *Science* **280**, 1412–1415 (1998).
- [48] M. Berrill, Y. Wang, M. A. Larotonda, B. M. Luther, V. N. Shlyaptsev, and J. J. Rocca, “Pump pulse-width dependence of grazing-incidence pumped transient collisional soft-x-ray lasers,” *Phys. Rev. A* **75** (2007).
- [49] D. H. Martz, D. Alessi, B. M. Luther, Y. Wang, D. Kemp, M. Berrill, and J. J. Rocca, “High-energy 13.9 nm table-top soft-x-ray laser at 2.5 Hz repetition rate excited by a slab-pumped Ti:sapphire laser,” *Opt. Lett.* **35**, 1632–1634 (2010).
- [50] T. Ditmire, J. K. Crane, H. Nguyen, L. B. Dasilva, and M. D. Perry, “Energy-yield and conversion-efficiency measurements of high-order harmonic radiation,” *Phys. Rev. A* **51**, R902–R905 (1995).
- [51] C. G. Wahlstrom, J. Larsson, A. Persson, T. Starczewski, S. Svanberg, P. Salieres, P. Balcou, and A. Lhuillier, “High-order harmonic-generation in rare-gases with an intense short-pulse laser,” *Phys. Rev. A* **48**, 4709–4720 (1993).
- [52] K. Kondo, N. Sarukura, K. Sajiki, and S. Watanabe, “High-order harmonic-generation by ultrashort krf and tisapphire lasers,” *Phys. Rev. A* **47**, R2480–R2483 (1993).



BIBLIOGRAPHY

- [53] G. Sommerer, E. Mevel, J. Hollandt, D. Schulze, P. V. Nickles, G. Ulm, and W. Sandner, "Absolute photon number measurement of high-order harmonics in the extreme UV," *Opt. Commun.* **146**, 347–355 (1998).
- [54] M. Schnurer, Z. Cheng, M. Hentschel, G. Tempea, P. Kalman, T. Brabec, and F. Krausz, "Absorption-limited generation of coherent ultrashort soft-X-ray pulses," *Phys. Rev. Lett.* **83**, 722–725 (1999).
- [55] D. Gabor, "A New Microscopic Principle," *Nature* **161**, 777–778 (1948).
- [56] J. W. Goodman, *Introduction to Fourier Optics* (Roberts & Company Publishers, 2005), 3rd ed.
- [57] P. Hariharan, *Optical Holography: Principles, Techniques and Applications* (Cambridge University Press, 1985).
- [58] U. Schnars and W. Jueptner, *Digital Holography: Digital Hologram Recording, Numerical Reconstruction, and Related Techniques* (Springer, 2005).
- [59] D. Gabor and W. P. Goss, "Interference microscope with total wavefront reconstruction," *J. Opt. Soc. Am.* **56**, 849–858 (1966).
- [60] C. Knox, "Holographic microscopy as a technique for recording dynamic microscopic subjects," *Science* **153**, 989–990 (1966).
- [61] R. Bracewell, *The Fourier Transform and Its Applications* (McGraw-Hill, 2000).
- [62] B. Osgood, *Lecture Notes for EE 261 - The Fourier Transform and its Applications* (Stanford University, 2007).
- [63] H. A. Haus, *Waves and Fields in Optoelectronics* (Prentice-Hall, 1983).
- [64] E. N. Leith and J. Upatniek, "Wavefront Reconstruction With Continuous-Tone Objects," *J. Opt. Soc. Am.* **53**, 1377–1381 (1963).
- [65] O. Bryngdahl and A. Lohmann, "Single-Sideband Holography," *J. Opt. Soc. Am.* **58**, 620–624 (1968).
- [66] T. Mishina, F. Okano, and I. Yuyama, "Time-alternating method based on single-sideband holography with half-zone-plate processing for the enlargement of viewing zones," *Appl. Opt.* **38**, 3703–3713 (1999).

BIBLIOGRAPHY

- 
- [67] C. Ramirez, A. Lizana, C. Iemmi, and J. Campos, “Inline digital holographic movie based on a double-sideband filter,” *Opt. Lett.* **40**, 4142–4145 (2015).
- [68] I. Yamaguchi and T. Zhang, “Phase-shifting digital holography,” *Opt. Lett.* **22**, 1268–1270 (1997).
- [69] J. R. Fienup, “Phase retrieval algorithms - a comparison,” *Appl. Opt.* **21**, 2758–2769 (1982).
- [70] V. Elser, “Phase retrieval by iterated projections,” *J. Opt. Soc. Am. A* **20**, 40–55 (2003).
- [71] J. A. Rodriguez, R. Xu, C.-C. Chen, Y. Zou, and J. Miao, “Oversampling smoothness: an effective algorithm for phase retrieval of noisy diffraction intensities,” *J. Appl. Crystallogr.* **46**, 312–318 (2013).
- [72] C.-C. Chen, J. Miao, C. W. Wang, and T. K. Lee, “Application of optimization technique to noncrystalline x-ray diffraction microscopy: Guided hybrid input-output method,” *Phys. Rev. B* **76** (2007).
- [73] P. F. Almoró and S. G. Hanson, “Random phase plate for wavefront sensing via phase retrieval and a volume speckle field,” *Appl. Opt.* **47**, 2979–2987 (2008).
- [74] A. M. S. Maallo, P. F. Almoró, and S. G. Hanson, “Quantization analysis of speckle intensity measurements for phase retrieval,” *Appl. Opt.* **49**, 5087–5094 (2010).
- [75] P. Thibault, *Algorithmic Methods in Diffraction Microscopy* (Ph.D. Thesis - Cornell University, 2007).
- [76] S. H and Y. Y, *Vector space projections : a numerical approach to signal and image processing, neural nets, and optics* (Wiley-Interscience, 1998).
- [77] B. K. Chen, T. Y. Chen, S. G. Hung, S. L. Huang, and J. Y. Lin, “Twin image removal in digital in-line holography based on iterative inter-projections,” *J. Opt.* **18**, 065,602 (2016).
- [78] M. Howells, C. Jacobsen, J. Kirz, R. Feder, K. McQuaid, and S. Rothman, “X-ray holograms at improved resolution - a study of zymogen granules,” *Science* **238**, 514–517 (1987).

BIBLIOGRAPHY

- [79] P. Korecki, G. Materlik, and J. Korecki, “Complex gamma-ray hologram: Solution to twin images problem in atomic resolution imaging,” *Phys. Rev. Lett.* **86**, 1534–1537 (2001).

